

THESIS

PERFORMANCE AND PLUME CHARACTERIZATION OF A LABORATORY KRYPTON HALL
THRUSTER

Submitted by

Thomas Malachi Andreano

Department of Mechanical Engineering

In partial fulfillment of the requirements

For the Degree of Master of Science

Colorado State University

Fort Collins, Colorado

Spring 2020

Master's Committee:

Advisor: John D. Williams

Anthony J. Marchese

Jacob L. Roberts

Copyright by Thomas M. Andreano 2020

All Rights Reserved

ABSTRACT

PERFORMANCE AND PLUME CHARACTERIZATION OF A LABORATORY KRYPTON HALL THRUSTER

Hall thruster research has been in progress at the CSU Electric Propulsion and Plasma Engineering (CEPPE) lab for the past decade, however, a full performance and plasma plume characterization has not been conducted with the laboratory Hall thruster available, which recently was modified to be configured as magnetically shielded as well as non-magnetically shielded. Additionally, heaterless cathode geometries that could benefit scaling of Hall thrusters to either much larger or much smaller designs have been undergoing development at the CEPPE lab. One of these cathodes, named the postage stamp, was designed to mount to the outer pole piece on the front of the thruster in the separatrix of the magnetic field, and fits in the space between the outer pole piece and the backplate of the thruster. To further the research on Hall thrusters at CSU, a baseline of the laboratory thruster performance is necessary, and performance characterization of the operation using different cathodes is necessary to further the cathode design. To these ends, performance of the thruster was characterized with: (1) the center mounted cathode, providing a baseline for all future Hall thruster research at the CEPPE lab, (2) with the postage stamp cathode, to determine the potential performance differences between operation with the two cathodes, and (3) in the magnetically shielded configuration, to verify proper operation and investigate any potential performance differences compared to the traditional configuration. Thrust measurement, along with data from an Electrostatic Analyzer (ESA), $E \times B$ probe, and Faraday probe were collected to determine the performance characteristics of the thruster as well as the characteristics of the ion beam in each of the three cases outlined above. Additionally, a preliminary study of an anomalous operation mode providing higher than usual performance was conducted using these probes, as well as a combined ESA/ $E \times B$ called the EVADER probe.

ACKNOWLEDGEMENTS

First, I would like to thank my advisor, Dr. John Williams, for the immense amount of support, guidance and mentorship throughout my time at Colorado State. Dr. Williams' energy and excitement about the work done in his lab is inspiring. I would also like to thank the other members of my committee, Dr. Anthony J. Marchese and Dr. Jacob Roberts, for their support and guidance in the formation and completion of this thesis.

I would also like to thank the other members of our lab group, each of whom have been incredible people to work with over the past two years. Seth Thompson was a source of frequent advice and knowledge on cathodes, plasmas, and coffee. Ryan Ham's patience and talent for explaining difficult concepts was a large part of my passing MECH 568. Casey, Cody, and Shawn Farnell helped me through frustrating mechanical and electrical troubleshooting problems more times than I can count, and I truly will never be able to thank them enough for everything I've learned from them. Jack VanGemert, Malcolm Roux, and Susan Ossareh provided laughs and great conversation. I also had the pleasure of working with Morgane Clement, Davide Morfei, and Maxime Saumier, three international scholars working in our lab over the course of my graduate career. These three were instrumental in the completion of this research, and working with them, learning about their respective countries and having people to bounce ideas off of was one of the largest sources of joy during my time at CSU. Last but not at all least, Daisy Williams played a large part in the completion of this thesis, keeping all of us in the lab in-line and on task.

Finally, I'd like to thank my family and friends. My mother, Nancy Andreano, provided support and encouragement during my hardest times. My father, Larry Andreano, was always interested in hearing the technical details of my research. My sister, Jacquie Andreano, was invaluable as an open ear for venting frustrations. And I never would have gotten through without the constant support of a multitude of friends, you all have my eternal gratitude.

TABLE OF CONTENTS

ABSTRACT	ii
ACKNOWLEDGEMENTS	iii
LIST OF TABLES	vi
LIST OF FIGURES	vii
Chapter 1 Introduction	1
1.1 Electric Propulsion	1
1.2 Hall Thruster Physics and Operation	3
1.3 Laboratory Hall Thruster Performance	4
1.4 Heaterless Cathodes	7
1.5 Plasma Diagnostics	9
1.5.1 Faraday Probe	9
1.5.2 Electrostatic Analyzer	10
1.5.3 E×B Probe (Wien filter)	11
1.5.4 EVADER probe	12
1.6 HET High Performance Mode of Operation	13
Chapter 2 Experimental Apparatus	15
2.1 Laboratory Hall Thruster	15
2.1.1 Traditional Configuration	15
2.1.2 Magnetically Shielded Configuration	16
2.2 Heaterless Cathodes	18
2.3 Vacuum Facility	20
2.4 Thrust Stand	22
2.5 Plasma Diagnostics	24
Chapter 3 Analysis Methods	29
3.1 Faraday Probe Data Analysis	29
3.2 Electrostatic Analyzer Data Analysis	31
3.3 E×B Probe Data Analysis	32
Chapter 4 Test Procedure and Results	34
4.1 Procedure	34
4.2 Test Results	35
4.2.1 Performance Comparison with Two Cathodes	35
4.2.2 Magnetically Shielded Thruster Performance	53
4.3 High Performance Mode of Operation	64
Chapter 5 Conclusion and Future Work	71
5.1 Conclusion	71
5.2 Future Work	73
5.2.1 Further Investigation of the High Performance Mode	73

5.2.2	Magnetic Field Mapping	73
5.2.3	Magnetically Shielded Thruster Plume Characterization	74
5.2.4	Hall Current Tomography	74
5.2.5	Thruster upgrades	74
Bibliography		76

LIST OF TABLES

4.1	April 2019 test using the center-mounted cathode	40
4.2	April 2019 test using the postage stamp cathode	40
4.3	February 2020 test using the center-mounted cathode	53
4.4	February 2020 test using the postage stamp cathode	53
4.5	March 2020 test using the magnetically shielded configuration	64
4.6	High performance operation mode data set	70

LIST OF FIGURES

1.1	Schematic of Hall thruster operation, taken from [1]	3
1.2	Model of the Faraday probe used in these efforts	10
1.3	Comparison of the current trace recorded by the E×B and EVADER probes	13
2.1	CSU Hall thruster with center mounted and pole-piece mounted cathodes	16
2.2	Backplates of both the standard and magnetically shielded configurations of the CSU HET	17
2.3	FEMM simulation of the MS thruster	17
2.4	Section view of the new center mounted cathode 3D model	18
2.5	Section view of the CSU HET 3D model with new center mounted cathode	19
2.6	Section view of the of the postage stamp cathode 3D model	20
2.7	Schematic of the vacuum chamber used for this research	20
2.8	Circuit diagram for the Hall thruster	21
2.9	Thrust stand with the HET mounted	22
2.10	Schematic of the LVDT used for measuring displacement of the thrust stand	23
2.11	E×B and EVADER probes mounted to the 4DOF motion stage	24
2.12	Circuit diagram for the E×B, provided by Plasma Controls, LLC	25
2.13	Circuit diagram for the ESA, provided by Plasma Controls, LLC	26
2.14	Circuit diagram for the EVADER probe, provided by Plasma Controls, LLC	27
2.15	Faraday probe and motion system	28
2.16	The magnetically filtered Faraday probe used for this research	28
3.1	Raw and corrected Faraday probe trace at 300V, 4.75 mg/s with the center-mount cathode	30
3.2	ESA trace at 300V, 4.75 mg/s with the center-mount cathode	31
3.3	E×B probe trace at 300V, 4.75 mg/s with the center-mount cathode	32
4.1	Thrust as a function of discharge voltage and anode mass flow-rate for the April 2019 data-set	36
4.2	Anode efficiency as a function of discharge voltage and anode mass flow-rate for the April 2019 data-set	38
4.3	Anode specific impulse as a function of discharge voltage and anode mass flow-rate for the April 2019 data-set	39
4.4	CSU Hall thruster operating during the February 2020 test campaign	41
4.5	Thrust as a function of discharge voltage and anode mass flow-rate for the February 2020 data-set	42
4.6	Anode efficiency as a function of discharge voltage and anode mass flow-rate for the February 2020 data-set	44
4.7	Anode specific impulse as a function of discharge voltage and anode mass flow-rate for the February 2020 data-set	45
4.8	ESA traces at 300V, 4.75 mg/s with the center-mount and postage stamp cathodes	46

4.9	Voltage utilization efficiency calculated with the most probable energy and average energy vs. discharge voltage for the HET with the center-mount and postage stamp cathodes	47
4.10	Faraday probe traces at 300V, 4.75 mg/s with the center-mount and postage stamp cathodes	48
4.11	Current utilization and divergence efficiencies vs. discharge voltage for the HET with the center-mount and postage stamp cathodes	49
4.12	ESA traces at 300V, 4.75 mg/s with the center-mount and postage stamp cathodes . .	49
4.13	Charge and mass utilization efficiencies vs. discharge voltage for the HET with the center-mount and postage stamp cathodes	50
4.14	Anode efficiency vs. discharge voltage calculated using the thrust measurement, and the utilization efficiencies with the center-mount cathode	52
4.15	Anode efficiency vs. discharge voltage calculated using the thrust measurement, and the utilization efficiencies with the postage stamp cathode	52
4.16	Magnetically shielded configuration of the thruster running during the test campaign	54
4.17	Thrust as a function of discharge voltage and anode mass flow-rate for the magnetically shielded configuration and the traditional configuration (both using center mounted cathode)	56
4.18	Anode efficiency as a function of discharge voltage and anode mass flow-rate for the magnetically shielded configuration and the traditional configuration (both using center mounted cathode)	57
4.19	ESA traces at 300V, 4.75 mg/s with the traditional and magnetically shielded configurations, both using the center-mounted cathode	58
4.20	Voltage utilization efficiency calculated with the most probable energy and average energy vs. discharge voltage for the traditional and magnetically shielded configurations	59
4.21	Faraday probe traces at 275V, 4.75 mg/s with the traditional and magnetically shielded configurations	60
4.22	Current utilization and divergence efficiencies vs. discharge voltage for the HET in traditional and magnetically shielded configurations	61
4.23	$E \times B$ traces at 300V, 4.75 mg/s with the traditional and magnetically shielded configurations	61
4.24	Charge and mass utilization efficiencies vs. discharge voltage for the HET in traditional and magnetically shielded configurations	62
4.25	Anode efficiency vs. discharge voltage calculated using the thrust measurement, and the utilization efficiencies with the magnetically shielded configuration	63
4.26	Thrust, anode efficiency, and anode specific impulse in the high performance mode compared to nominal operation at 5.25 mg/s anode mass-flow rate	65
4.27	ESA probe trace at 300V, 5.25 mg/s in the high performance mode and nominal operation	66
4.28	Comparison of the $E \times B$ probe trace at 300V, 5.25 mg/s during nominal operation and in the high performance mode	67
4.29	EVADER probe traces at selected ion energies in the high performance mode at 300V, 5.25 mg/s	68

4.30	Current utilization and divergence efficiencies vs. discharge voltage for the HET in high performance mode and nominal operation	69
4.31	Anode efficiency vs. discharge voltage calculated using the thrust measurement, and the utilization efficiencies for the high performance data-points	70

Chapter 1

Introduction

The aim of this research was to perform an in-depth characterization of the Colorado State University (CSU) Electric Propulsion and Plasma Engineering (CEPPE) laboratory Hall-effect thruster through the investigation of performance and plasma plume characteristics associated with operating the thruster using a center mounted cathode, using a planar-style cathode mounted to the outer pole-piece of the Hall thruster, and lastly with the thruster in a magnetically shielded configuration. In the course of this study, a mode of thruster operation providing higher thrust, specific impulse, and efficiency than normal operation was discovered when applying higher current to the magnetic circuit, and so the second goal of the research was to investigate this high performance operation mode. To understand the performance of the thruster, a suite of plasma diagnostic probes was set up within the vacuum chamber. Two sets of test data with each of the cathode configurations were collected over the course of a year, and one set of test data was collected with the magnetically shield configuration.

1.1 Electric Propulsion

Electric propulsion (EP) is a category of in-space propulsion that relies on electric power supplies to add energy to and accelerate a propellant away from the spacecraft, creating thrust. This can provide a benefit compared to chemical propulsion, as the latter is limited in the ability to attain high propellant exhaust velocity by the quantity of energy stored in molecular bonds and the materials used in the combustion chamber and nozzle. In contrast, electric propulsion is only limited by the energy that can be created by a power system on the spacecraft, making power system technology (photovoltaic solar power arrays, nuclear reactors, etc.) and scaling laws the only limiting factors. In addition, electric propulsion systems can be used to accelerate propellants to much higher exhaust velocities than chemical propulsion [1], leading to higher specific impulse, often described as analogous to "gas mileage". This allows the propellant

mass for any given mission to be lowered, a critical consideration in space due to the cost of launching mass out of Earth's atmosphere.

Though not used in space until 1964, electric propulsion was first briefly mentioned in a publication more than 50 years prior by Konstantin Tsiolkovsky in 1911 [2].

It is possible that in time we may use electricity to produce a large velocity for the particles ejected from a rocket device.

Tsiolkovsky later elaborated slightly on this idea in 1924, but ultimately deemed that it was not currently feasible with the technology of the time [2]:

It is quite probable that electrons and ions can be used, i.e. cathode and especially anode rays. The force of electricity is unlimited and can, therefore, produce a powerful flux of ionized helium to serve a spaceship. However, we shall leave these dreams for a while and return to our prosaic explosives.

However, some theoretical work on electrostatic thrusters was done by Robert Goddard in the 1910's, and in 1917 he filed a patent for an electrostatic ion accelerator [3]. EP gained authority in 1929 when Hermann Oberth published his seminal work *Wege zur Raumschiffahrt*, including an entire chapter on electric space propulsion and power [4]. By the 1960's, large research programs were created in government and academia for electric propulsion, and the first flight tests of EP were conducted in 1964 using ablative pulsed plasma thrusters [5]. Since then, electric propulsion has blossomed into a mature and prolific technology, with hundreds of spacecraft currently utilizing EP in space [6].

Several subcategories of electric propulsion exist, mainly: electrostatic, in which charged particles are accelerated by an applied electric field, electromagnetic, in which the propellant is accelerated by a combination of applied electric and magnetic fields, and electrothermal, in which electrical power is used to heat a propellant to accelerate its flow. Electrostatic propulsion systems include gridded ion thrusters, Hall-effect thrusters, and electrospray thrusters. Electromagnetic systems include, magnetoplasmadynamic thrusters (MPDs), helicon thrusters, and Lorentz force thrusters. Electrothermal propulsion systems include arcjet and resistojet thrusters.

1.2 Hall Thruster Physics and Operation

The focus of this research is Hall-effect thrusters (HETs), which make use of strong, primarily radial magnetic fields and primarily axial electric fields created within an annular channel for ionization and acceleration of a propellant. Figure 1.1 contains a cross-section schematic of a HET, describing the field vectors and motion of the neutrals, ions, and electrons.

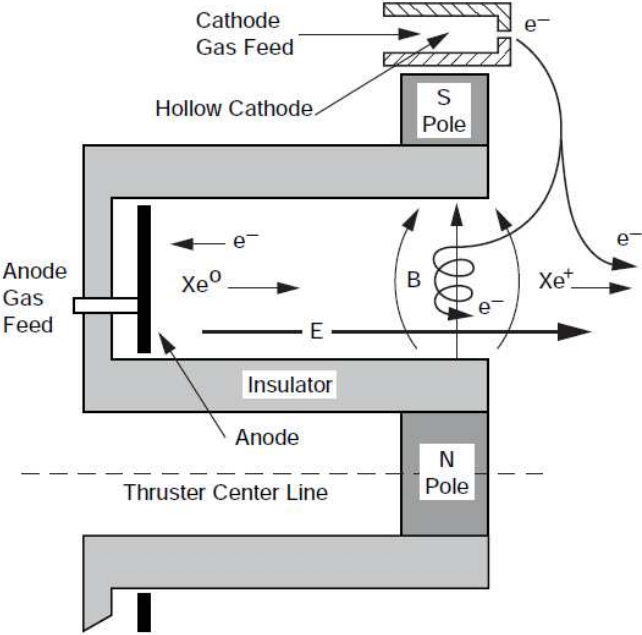


Figure 1.1: Schematic of Hall thruster operation, taken from [1]

Electrons, attracted toward the high positive potential of the anode located at the upstream end of the channel, move from the cathode into the discharge channel but are quickly repressed by the strong, mostly radial magnetic field near the downstream end of the channel. The electrons move gyroscopically around the magnetic field lines as shown in Fig. 1.1, but also experience the Lorentz force due to the perpendicular E and B fields. This force is in the E×B direction, forcing the electrons into a circular motion around the channel and restricting their direct path to the anode [1] and providing an increased opportunity for collisions with propellant molecules and thus, ionization. This circulating movement of the electrons creates an

embedded current referred to as the Hall current. Propellant ions created at high positive electric potentials inside the channel are accelerated to high exhaust velocities by the axial electric field, creating thrust force on the HET, and thus on the spacecraft. Hall thrusters are categorized as electrostatic thrusters because the propellant ions are accelerated by the electric field present in the channel of the thruster, and are not affected by the radial magnetic field, as the electrons are, due to their high mass [1].

1.3 Laboratory Hall Thruster Performance

Laboratory Hall thruster performance is characterized using derived metrics based on measurements of several operating parameters of the propulsion system. These measured or recorded parameters are typically thrust, power, and mass-flow rate. In a lab setting, thrust is directly measured by a thrust stand, while voltage and current values are recorded directly from the power supplies in use, and the mass-flow rate of the propellant is measured by mass-flow controllers. Commonly, losses due to non-optimized magnetic circuit or cathode operation are discarded when characterizing the performance of a laboratory hall thruster, and "anode" metrics are used to allow focus on the plasma production and acceleration processes [1]. The primary metrics used to characterize the performance of any Hall thruster are thrust, T , specific impulse, I_{sp} , and efficiency, η . When comparing performance between propulsion systems, thrust to power ratio is also a commonly used metric, but was not focused on in this work.

The force on a system is defined as the time rate of change of momentum of the system, so the thrust force created by a propulsion system, in which the only change in mass is from the expelled propellant, is described by Equation 1.1, where T is thrust, \dot{m}_p is the propellant mass-flow rate, and v_{ex} is the exhaust velocity of the propellant [1].

$$T = \frac{d}{dt}(m_p v_{ex}) = \dot{m}_p v_{ex} \quad (1.1)$$

Specific impulse is a concept unique to rocket propulsion, and is defined as the thrust produced per weight-flow-rate of propellant [7] (or impulse per unit weight of propellant). Though

not entirely an accurate analogy, specific impulse is often compared to gas-mileage for earth-bound vehicles, as it provides a measure of the change in velocity, ΔV , capabilities of the propulsion system for a given amount of propellant. A thruster with a higher specific impulse requires a smaller propellant mass for a given mission ΔV . The anode specific impulse is found by neglecting mass flow to all components other than the anode, \dot{m}_a . Total specific impulse, I_{sp} , and anode specific impulse, $I_{sp,anode}$, are then given by Equations 1.2 and 1.3, respectively, where g_0 is standard gravitational acceleration.

$$I_{sp} = \frac{T}{\dot{m}g_0} = \frac{v_{ex}}{g_0} \quad (1.2)$$

$$I_{sp,anode} = \frac{T}{\dot{m}_a g_0} \quad (1.3)$$

Total thruster efficiency is defined as the jet power of the beam divided by the total power input to the Hall thruster. Jet power, P_{jet} , is the kinetic power of the beam and is described mathematically by Equation 1.4 [1]. The total efficiency of the thruster is then given by Equation 1.5, where P_{in} is the total power input to the thruster.

$$P_{jet} = \frac{1}{2} \dot{m}_p v_{ex}^2 = \frac{T^2}{2\dot{m}_p} \quad (1.4)$$

$$\eta_T = \frac{T^2}{2P_{in}\dot{m}_p} \quad (1.5)$$

As mentioned previously, it is common to report the anode efficiency when dealing with laboratory thrusters. Similarly to anode specific impulse, the anode efficiency is found by neglecting power and mass flow to all components other than the anode, giving Equation 1.6, where P_d is the power input from the discharge power supply (power input to the anode).

$$\eta_{anode} = \frac{T^2}{2P_d\dot{m}_a} \quad (1.6)$$

Thruster efficiency can also be broken down into several discrete process efficiencies, these being the current utilization efficiency, divergence efficiency, voltage utilization efficiency, charge utilization efficiency, and mass utilization efficiency. Current utilization efficiency, η_b , is simply the fraction of discharge current, I_d , that is converted into beam current, I_b , and can be calculated using Equation 1.7 [1].

$$\eta_b = \frac{I_b}{I_d} \quad (1.7)$$

Plume divergence affects the overall efficiency of thruster operation because ions whose energy is not directed in a straight line from the thruster do not contribute their whole energy to production of thrust along the axis of the thruster. Plume divergence angle, δ , is usually defined as the half-angle in which 95% of the beam current is contained. Divergence efficiency, η_d , is defined as the cosine of the divergence angle squared, shown by Equation 1.8 [8, 9].

$$\eta_d = (\cos\delta)^2 \quad (1.8)$$

Voltage utilization efficiency, η_v , is defined as the average accelerating potential, \overline{V}_b , applied to the ions divided by the discharge voltage, V_d . The average accelerating potential is typically defined as the loss voltage, V_l , subtracted from the discharge voltage, where the loss voltage is calculated as the difference between the discharge voltage and the most probable ion energy [10]. Thus, the voltage utilization efficiency can be described mathematically by Equation 1.9 [1].

$$\eta_v = \frac{\overline{V}_b}{V_d} = 1 - \frac{V_l}{V_d} \quad (1.9)$$

The charge utilization efficiency, η_q , is a measure of the fraction of multiply charged ions in the beam, shown by Equation 1.10 [10], where f_i is the fraction of beam current of a given charge species, and Z_i is the charge state of the species.

$$\eta_q = \frac{(\sum \frac{f_i}{\sqrt{Z_i}})^2}{\sum \frac{f_i}{Z_i}} \quad (1.10)$$

Mass utilization efficiency, η_m , is calculated by dividing the ion beam mass-flow rate, \dot{m}_b , by the anode mass-flow rate, \dot{m}_a . Ion beam mass-flow rate for a beam consisting of only singly charged ions can be found by multiplying the beam current by the propellant molecular mass and dividing by the elementary charge. However, the presence of multiply charged ions must be taken into account to determine the actual mass-flow of beam ions. Thus, measurements of the charge state of the ions as well as the beam current are required, and the mass utilization efficiency is calculated with Equation 1.11, where ζ is the conversion ratio of anode mass flow to propellant current [10].

$$\eta_m = \frac{\dot{m}_b}{\dot{m}_a} = \zeta \eta_b \sum \frac{f_i}{Z_i} \quad (1.11)$$

These separate utilization efficiencies can then be combined into another formulation of the thruster anode efficiency, displayed by Equation 1.12 [10].

$$\eta_{anode} = \eta_b \eta_d \eta_v \eta_m \eta_q \quad (1.12)$$

Determining each of these utilization efficiencies gives important insight into which processes are impacting the overall efficiency of the thruster the most, and is thus an important part of Hall thruster characterization.

1.4 Heaterless Cathodes

The cathode is a critical part of the overall operation of a HET, as it is used to produce the electrons that both initialize the plasma discharge in the thruster channel as well as neutralize the ion beam expelled from the thruster. Hall thrusters typically utilize hollow cathodes with an integrated heating element to thermally prime a low work function insert before operation. The heating element takes the form of a resistive coil wrapped around the cathode tube that is itself

nested within heat radiation shielding and an enclosed keeper assembly. A dedicated power supply drives an electric current through the heater, heating the cathode until the insert begins to thermionically emit electrons and, shortly thereafter, produce a plasma discharge through the action of power supplies that bias the keeper and anode electrodes positive relative to the cathode. The cathode heater power supply is one of five supplies used to start and operate a Hall thruster – two supplies for the inner and outer electromagnets, which shape the magnetic field structure, a fourth supply powers the keeper during ignition, and a fifth biases the anode to maintain the plasma discharge. Through the introduction of a heaterless hollow cathode (HHC), the cathode heater power supply can be removed, simplifying the Hall thruster system. HHCs, in addition, eliminate a potential area of failure by removing the heater element that is susceptible to thermal-cycle fatigue and electro-thermal degradation [11].

The mechanisms of HHC ignition are well explained in [11–13]. Aston conducted an early study of a HHC in 1981 using a refractory cathode tube to produce a “microplasma” discharge [14]. Notable in Aston’s cathode configuration was the omission of a low work function insert to aid in the initiation and operation of the cathode. Research was later conducted on HHCs with impregnated inserts [12, 15–17]. Several studies, predominantly from outside the U.S., have sought insight into the effects of HHCs when used with Hall thrusters [16, 18–22]. HHCs using versions of a barium-impregnated insert have been reported being used with an SPT-100 thruster [16, 18], and Loyan et al. tested a HHC at a center-mounted position and an external position near the separatrix [21]. Mounting the cathode near the separatrix has been suggested by both Hofer et al. and Sommerville et al [23, 24]. In addition, Jameson et al. found a 2-3% increase in total efficiency of a Hall thruster when moving from an externally mounted cathode to an internally mounted cathode [25].

A number of formulations for the barium-impregnated insert are used in hollow cathodes that are produced commercially through a series of complex processes, which are reflected in the high cost of these inserts. A partnership between Colorado State University and Plasma Controls, LLC, has enabled the production of barium-based, ceramic-metal composite (cermet)

inserts made with an alternative, streamlined process resulting in low work function cathode inserts of comparatively lower cost. The nature of the process along with the close proximity of these partnered institutions have allowed for flexibility in the development of hollow cathodes of varying sizes and configurations with cermets of customizable compositions [26].

1.5 Plasma Diagnostics

Of much interest in the field of Hall thrusters are the properties of the near and far field plasma plume, including the beam current, ion energy distribution, and charge state ratio. This information can be measured through the use of various probes that are common in the field of plasma physics in general, and several of these probes, the Faraday probe, electrostatic analyzer, and E×B probe, will be discussed in the following pages. In addition, a lesser known diagnostic system in development, called the EVADER probe by Plasma Controls LLC, will be discussed.

1.5.1 Faraday Probe

The Faraday probe is a simple diagnostic probe used for measuring the current of ions in the plasma plume. A conductor is placed in the beam and biased to a negative voltage to attract ions and repel electrons. The conducted current of ions is then measured by an ammeter. Typically, the probe is moved in an arc at a set radius from the thruster to capture a trace of the current density across the entire plasma plume. This measured current density can then be integrated on the spherical surface corresponding to the arc traveled by the probe to calculate the total beam current, as shown by Equation 1.13, where R_{fp} is the radius from the center of the thruster face to the probe, j is the current density, and θ is the angle of the probe relative to the center axis of the thruster. The beam current is used to calculate the current utilization efficiency of the thruster [8, 27].

$$I_b = 2\pi R_{fp}^2 \int_0^{\pi/2} j(\theta) \sin\theta d\theta \quad (1.13)$$

A 3D model of the Faraday probe used in this research is shown in Fig. 1.2 below. For this research the addition of two small permanent magnets to the outer guard ring was included to assist in the repelling of electrons. This configuration was first used at the University of Michigan and is detailed in [28].



Figure 1.2: Model of the Faraday probe used in these efforts

1.5.2 Electrostatic Analyzer

An electrostatic analyzer (ESA) separates ions in the plasma plume based on their energy per charge. In the spherical deflector ESA used for this research, ions in the beam enter the probe and move into a region between two spherical segments that are biased to potentials that create an electric field between the segments, which exerts a force on the ions traveling through the segment. The potential difference between the two plates determines the necessary energy an ion must have to make it unhindered through the region. If the velocity of the ion is too low or too high, it will drift toward the plates and will not pass through the collimator at the end of the segment, and thus will not be collected as current by the collector [29, 30].

Data collected from the ESA are analyzed by calculating the average energy of the ions, the most probable energy of the ions (the peak of the current trace), and the full width at half max. These metrics give a general sense of the ion acceleration process, the spread of ion energies, and the average and/or most probable ion energy can be used to calculate the voltage utilization efficiency.

1.5.3 $E \times B$ Probe (Wien filter)

The $E \times B$ (pronounced E cross B) probe, also known as a Wien filter, separates ions based on their charge state, mass, or energy. In the field of electric propulsion, $E \times B$ probes are typically used to calculate the relative concentrations of singly, doubly, and triply ionized propellant atoms in the plume. Plume ions enter the probe and travel into the separation segment where two plates are biased to create a potential difference between the plates. A magnetic field perpendicular to the applied E-field is also created by permanent magnets in this section, so that a Lorentz force is exerted on the ions. The Lorentz force is described by Equation 1.14, where F is the force exerted on the charged particle, q is the magnitude of the particle's charge, E is the magnitude of the electric field, v is the velocity of the particle, and B is the magnitude of the magnetic field.

$$F = q(E + v \times B) \quad (1.14)$$

The ions can only make it through the segment to the collector if the force they feel is nearly zero, so the forces on the ion due to the electric and magnetic fields must be equal. Thus, for a given electric and magnetic field, the collection of ions is governed by the ion's velocity, which is related to the charge state, z , mass, m , and the potential difference between the probe entrance and the point in the plasma where the ion was created, ΔV_p . Equation 1.15 gives the ion's velocity as it enters the probe [31].

$$v = \sqrt{\frac{2 \cdot z \cdot q \cdot \Delta V_p}{m}} \quad (1.15)$$

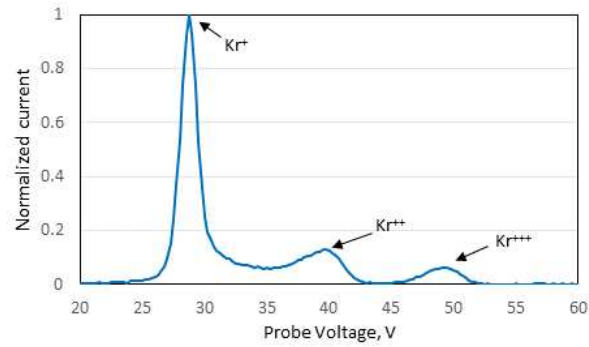
From Equation 1.15 it can be seen that if all ions are the same (or nearly the same) mass and are created at the same potential, the charge state of the ion is the determining factor in whether the ion is collected after passing through a given segment potential. The bias on the two plates is swept through a range of voltages to ensure at the very least singly, doubly, and

triply charged ions are collected, and the resulting distribution can then be used to calculate the relative ratio of charge states of the beam ions.

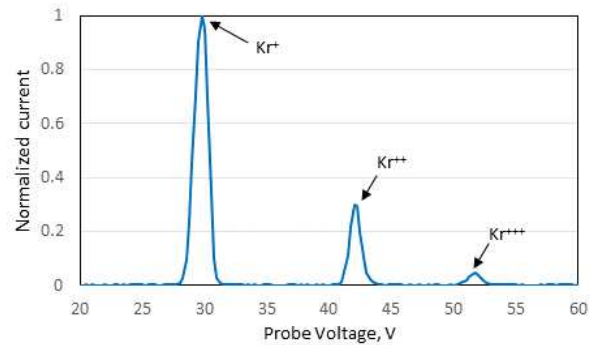
Analysis of the data from an $E \times B$ can be done using several methods [32], but the general aim is to integrate the current under each of the current peaks that signify each charge state species. Then the ratio of doubly and triply charged ions to singly charged ions can be calculated. Typically, numerical methods are used to integrate the current, and for this research the triangular method was chosen, which approximates the area under each peak as a triangle with height equal to the peak and base equal to the full width at half max (FWHM) to find the area under the curve [32, 33].

1.5.4 EVADER probe

The Energy and Velocity Analyzer for Distributions of Electric Rockets (EVADER) probe, developed by Plasma Controls, LLC, combines the functions of an ESA and an $E \times B$ probe, allowing charge state separation at specific energy bands. Hall thruster ion energy distribution functions often include "shoulders" of high and/or low energy ions above and below the discharge voltage, which causes 'blending' between the peaks in $E \times B$ probe traces since the ions are not all created at the same potential. Insight into the charge state ratios of these high and low energy ions provides information on where and how high or low energy ions are created. The traces provided by the EVADER probe are much easier to analyze compared to traditional $E \times B$ probe traces, since the ion current is monoenergetic. Examples of traces from a traditional $E \times B$ and from the EVADER probe are shown below in Fig. 1.3 to highlight the improvement of the latter for ease of analysis.



(a) E×B probe trace



(b) EVADER probe trace

Figure 1.3: Comparison of the current trace recorded by the E×B and EVADER probes

1.6 HET High Performance Mode of Operation

Typically in laboratory Hall thruster testing it is standard to adjust the current(s) supplied to the electromagnetic coils of the magnetic circuit, thus adjusting the magnetic field strength, so as to minimize the discharge current for a set discharge voltage and anode mass-flow rate. This theoretically provides the optimal efficiency for a given mass-flow and discharge voltage [7].

In the course of laboratory thruster testing for this research, it was noticed that a higher coil current, thus higher magnetic field strength, created a pronounced difference in the brightness of the plasma plume, corresponding to an increase in discharge current. What was interesting about this mode was that the thrust also increased, enough to make up for the increased power input, and so efficiency and specific impulse increased as well by values up to 20% greater than values found using the discharge current minimization method described in [7]. Subsequently,

an investigation to understand the mechanisms behind this increased thrust production that resulted in not only higher thrust, but also higher efficiency and specific impulse was conducted.

Chapter 2

Experimental Apparatus

2.1 Laboratory Hall Thruster

2.1.1 Traditional Configuration

The CSU Hall thruster is a stationary plasma thruster (SPT) style thruster capable of operation under input power from 1 to 2 kW, and designed for nominal operation at 1.5kW (300V, 5A discharge). The thruster is designed based on the SPT-100D and uses a single inner electromagnetic coil and four discrete outer electromagnetic coils to create the magnetic field necessary for Hall-effect thruster operation. The magnetic circuit is designed to create a "plasma lens" magnetic field that focuses the plasma plume and reduces beam divergence as described by [7]. The channel is annular, and was machined from borosil (BN-SiO₂), measuring 104 mm in outer diameter with a channel width of 17 mm and a channel length of 32 mm. The anode is made from stainless steel, and doubles as the propellant distributor. It sits at the upstream end of the borosil channel, cemented to the back wall of the channel with Sauereisen electrotemp cement. Three threaded rods that are fixed to the back of the channel pass through the backplate of the thruster so that the channel and anode can be mounted by tightening nuts onto the threaded rods. The center coil and the outer coils are mounted to the backplate of the thruster by socket head cap screws, and the outer pole piece is then mounted to the opposite side of the outer coils with four more socket head cap screws. The thruster was modified to incorporate both a center mounted hollow cathode, which mounts to the backplate of the thruster and is enclosed by the center magnetic coil, and a planar-style cathode that mounts directly to the outer pole piece of the thruster. The entire thruster is shown in Fig. 2.1, with both cathodes mounted.



Figure 2.1: CSU Hall thruster with center mounted and pole-piece mounted cathodes

At the beginning of this research effort, the Hall thruster was taken completely apart and thoroughly cleaned. All five magnetic coils were rebuilt using bare copper wire protected with a high temperature fiberglass sleeving made by Techflex, capable of heat resistance up to 1000 degrees Celsius. The center coil is further protected by a layer of Sauereisen electrotemp cement. The protected copper wire was wrapped around an iron core an appropriate number of times to achieve the desired magnetic field strengths using currents under the limit of the copper wire.

2.1.2 Magnetically Shielded Configuration

Several of the components of the HET were redesigned and fabricated to produce a magnetically shielded (MS) configuration of the thruster, where the magnetic field protects the channel walls from erosion as described in [34–36]. The outer pole piece and inner and outer shields for the magnetically shielded configuration feature bevels that shape the field into the correct topography to protect the channel walls from ion-induced sputter erosion. The backplates of the standard configuration and the magnetically shielded configuration are both shown in Fig. 2.2.

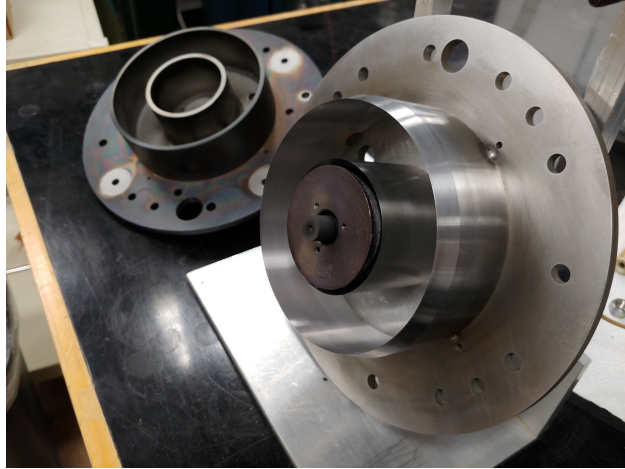


Figure 2.2: Backplates of both the standard and magnetically shielded configurations of the CSU HET

Finite Element Method Magnetics (FEMM) was used to model the magnetic field to design the components for the magnetically shielded configuration. An iterative process was used until the desired field, shown in Fig. 2.3, was accomplished. The modeled magnetic field was qualitatively matched to those described in [34–36].

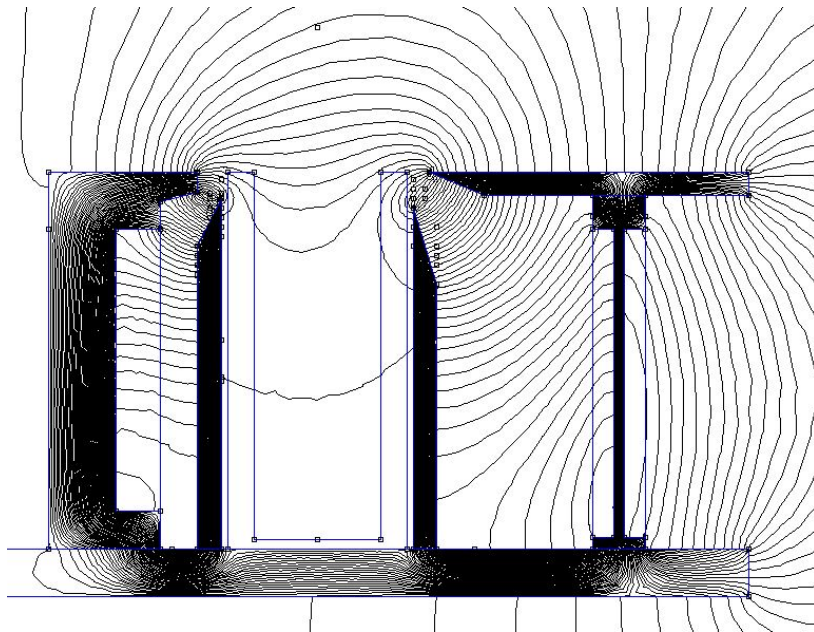


Figure 2.3: FEMM simulation of the MS thruster

2.2 Heaterless Cathodes

The hollow cathodes constructed for this study use low work function inserts made with a 5:3:2:0.5 formulation of BaO, CaO, Al₂O₃, and Sc₂O₃, respectively. The ceramic constituents were combined with tungsten powder in a patented process described by Farnell et. al [26] to produce the electron emitter cermet composite assembled in each cathode. Initially, the center mounted cathode was a hollow cathode of traditional tubular design which was made using a small-diameter, right-cylinder cermet insert installed at the downstream end of a 6.4 mm diameter Ta tube which was rolled down at the downstream end to form a hemispherical shaped orifice plate. The cathode tube orifice was 1.2 mm, and the cathode was center-mounted inside the core of the inner magnetic coil, but without an enclosed keeper assembly. Rather, the keeper electrode was a disk with a 3.75 mm orifice placed over the end of the hole in the inner magnet coil as patented by Martinez et. al. [37]. However, this cathode eventually failed and a new center mounted cathode was designed that uses an enclosed keeper assembly.

The new center mount cathode was designed based off of previous cathodes designed and built at the CEPPE lab, and features a graphite keeper enclosing a 0.25" tantalum cathode tube. A plug-style emitter was placed at the end of the tube, which was then crimped to hold the emitter in place. Two alumina silicate ceramics of 1/8th inch thickness isolate the keeper from the back of the thruster and from the base-plate of the cathode. The keeper orifice was drilled to a diameter of 0.08". A section view of the SolidWorks model of the new center mounted cathode is shown in Fig. 2.4, and a section view of the entire HET model including the cathode is shown in Fig. 2.5.

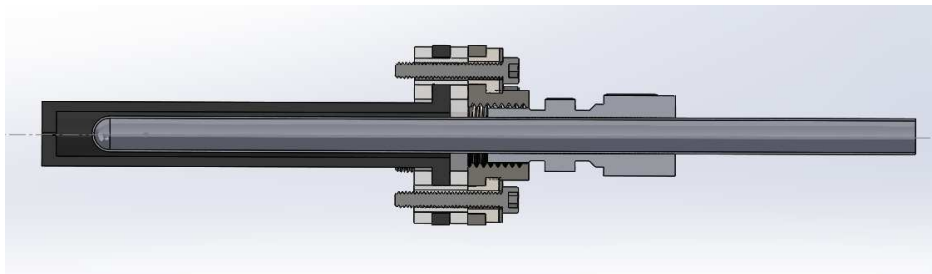


Figure 2.4: Section view of the new center mounted cathode 3D model

We note the lack of a cathode heater in our design, making this cathode of the heaterless variety that can be started instantly, without any conditioning or arming period. We also note the large spacing between the cathode tip and keeper orifice of 0.25". This large spacing facilitates the cathode start up [13].

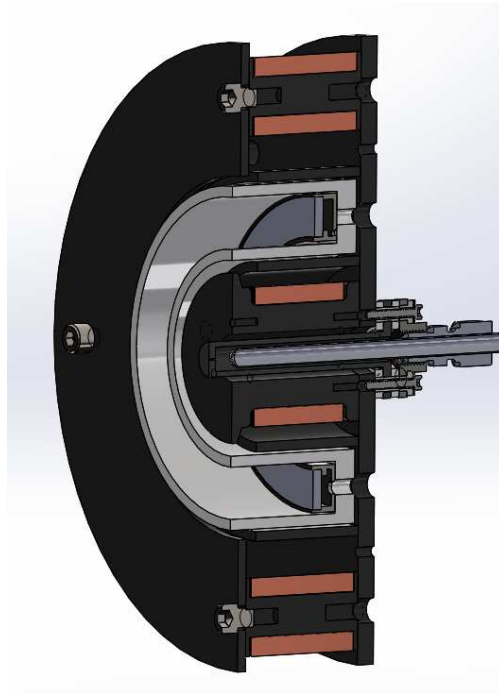


Figure 2.5: Section view of the CSU HET 3D model with new center mounted cathode

A second cermet was fashioned into a small disk with a diameter of 9 mm and a thickness of 2.5 mm and installed in the compact postage stamp cathode. The postage stamp, as seen in Fig. 2.6, has general envelope dimensions measuring 28.5 mm in diameter and 21 mm from the base-plate to the keeper orifice. Two alumina silicate plates separate the keeper from the base-plate, and the emitter is mounted to a sheet of thin tantalum foil sandwiched between the two ceramic plates. The keeper orifice diameter was drilled to a diameter of 0.06". When installed in the thruster, the downstream surface of the keeper for the postage stamp was positioned to be coincident with the plane of the outer pole piece with the keeper orifice located within the separatrix of the magnetic field structure as first demonstrated by Murashko et al [22].

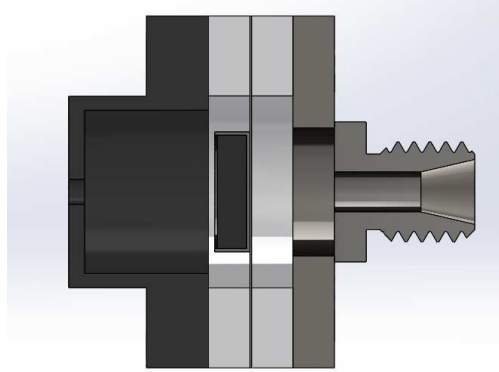


Figure 2.6: Section view of the of the postage stamp cathode 3D model

2.3 Vacuum Facility

A vacuum chamber measuring 1.7 m in diameter and 4.6 m in length was used for all tests. The chamber is equipped with a Leybold DryVac roughing pump, two Varian HS20 diffusion pumps, and two internal cryosails, the layout of which is shown in Fig. 2.7. The chamber is capable of reaching a base pressure of 8.0×10^{-7} Torr with a maximum pumping speed of 38,000 L/s on krypton. A graphite beam dump, located 2.8 m downstream of the thrust stand, separates the cryosails from direct exposure to the thruster plume.

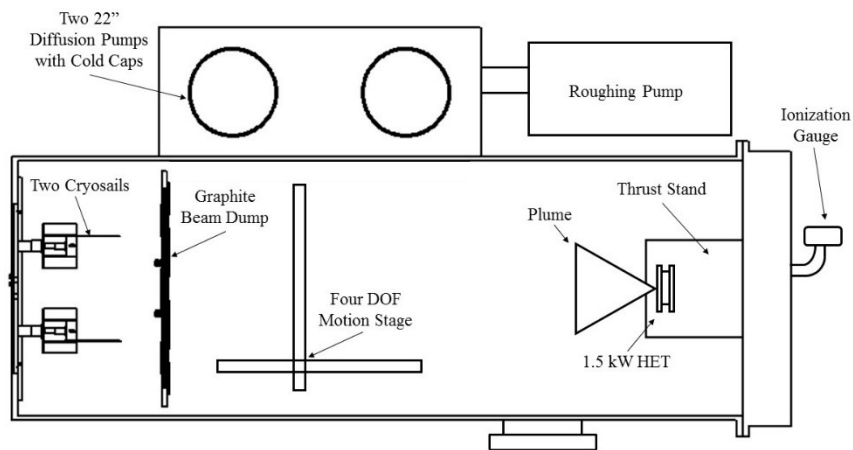


Figure 2.7: Schematic of the vacuum chamber used for this research

Four laboratory power supplies, with the notable absence of a cathode heater supply, were used to operate the HET. Both cathodes were installed so as to be electrically connected out-

side of the test chamber to allow for easy switching between the two. Two 100 ohm resistors in parallel were placed between the keeper and the cathode-keeper power supply to avoid excessive current flow at start-up. A 2.2 ohm resistor was wired in series with the anode and two oil tank capacitors each rated at 54 μF were wired in parallel to each other and placed in parallel between the anode and cathode to filter the anode power supply from plasma oscillations. The Hall thruster circuit diagram is shown in Fig. 2.8.

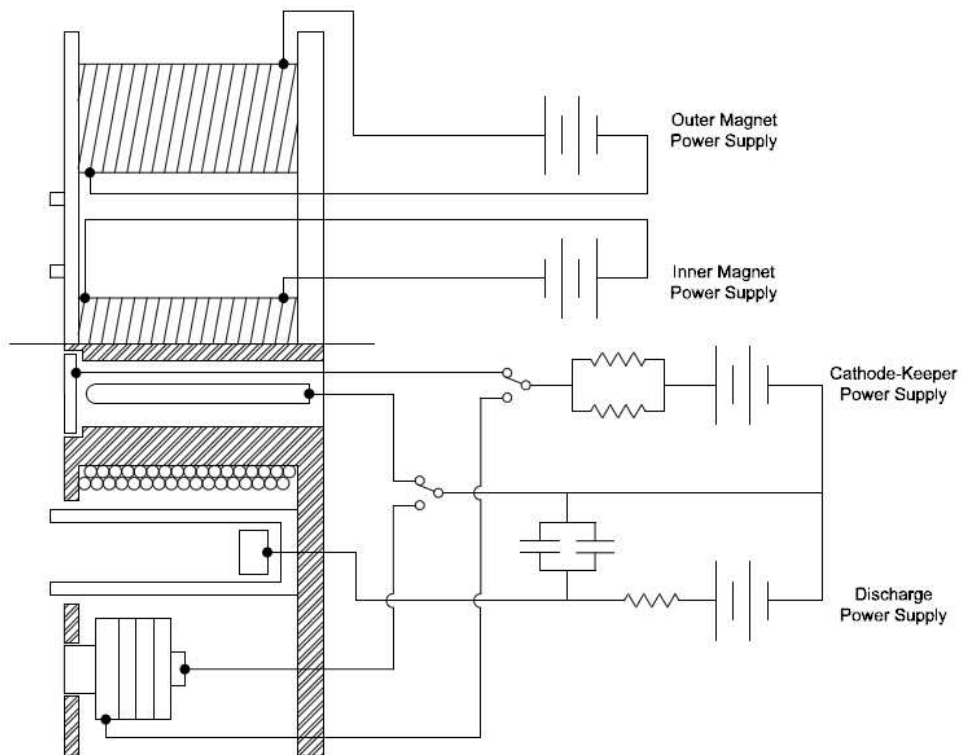


Figure 2.8: Circuit diagram for the Hall thruster

Blocking and freewheeling diodes were also included in the circuit to protect the keeper and anode power supplies from unstable operation. High-purity krypton gas (99.999%) was delivered to the anode and cathodes through three dedicated, stainless steel gas lines and controlled by 50 and 100 sccm mass flow controllers (used for the cathode and anode, respectively).

2.4 Thrust Stand

Thrust measurements were captured using a hanging double pendulum thrust stand. The main frame of the thrust stand is made of extruded aluminum, while the top and bottom plates of the hanging double pendulum are graphite. The pendulum is created through four stainless steel ribbons that connect the top and bottom plates. An eddy-current damper is used to dampen oscillation of the thrust stand. The thrust stand is shown in Fig. 2.9.

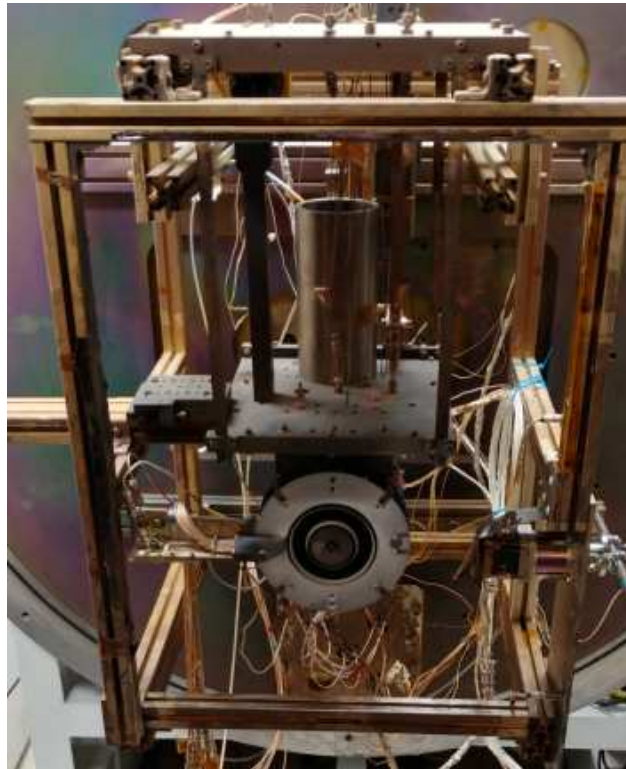


Figure 2.9: Thrust stand with the HET mounted

The 0.25" diameter stainless steel propellant lines run from the vacuum chamber door to the top plate of the stand where they are adapted to 0.0625" diameter tubes and are then configured in an accordion style before running through the bottom plate and to the thruster to minimize their affect on the motion of the stand. In addition, all wires and cables connected to the thruster are allowed to hang in a "waterfall" configuration to minimize their affect on the motion of the stand as well.

The stand uses a linear variable-differential transformer (LVDT) in combination with an SRS-810 lock-in amplifier to measure the displacement of the pendulum. The LVDT consists of a ferromagnetic core that is allowed to move linearly within the centers of three electromagnetic coils, with the two outer coils of the LVDT connected in series. A schematic of the LVDT is shown in Fig. 2.10.

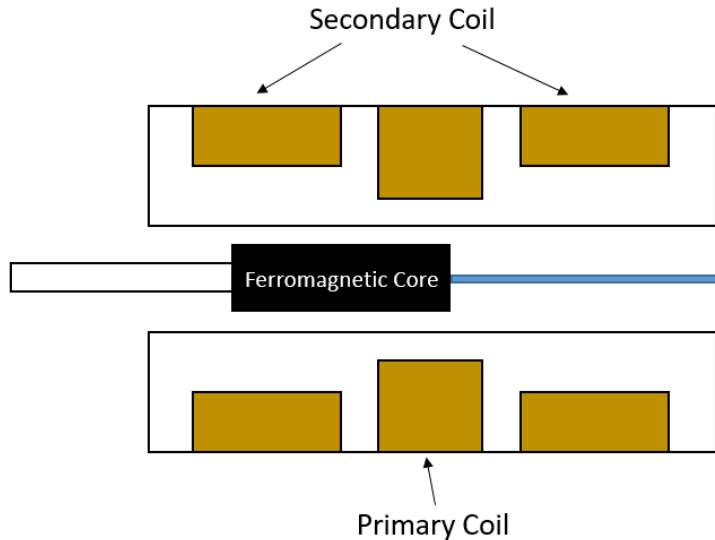


Figure 2.10: Schematic of the LVDT used for measuring displacement of the thrust stand

The lock-in amplifier provides an AC current at 15kHz to the center coil of the LVDT, while the displacement of the ferromagnetic core causes a voltage difference in the outer coils of the LVDT, which is picked up by the lock-in amplifier. Thus, the voltage difference created in the LVDT can be related to the displacement of the stand, and therefore can be related to the force created by the thruster, if calibrated using known applied forces beforehand. Calibration of the stand is achieved by applying known forces to the stand via a set of hanging weights and recording the voltage produced by the LVDT to create an equation relating the voltage measured by the LVDT and the applied force. The first weight is applied, the signal from the LVDT is recorded, and then the next weight is added. This is done for three weights, and is repeated a total of four times. To account for transient thermal effects, calibration is performed after running the

thruster for at least 2 hours, at which point it is assumed the system has reached thermal equilibrium. Calibration is repeated throughout extended test periods to maintain low error thrust measurements. A LabVIEW program is used for data acquisition and to send commands to the stepper motor used for moving the calibration weights. Error analysis is built in to the LabVIEW program, for which [38] was used as guidance.

2.5 Plasma Diagnostics

During testing, a suite of plasma diagnostic probes were used to provide insight into the performance of the thruster. As discussed in the preceding chapter, these probes are used to determine the average ion energy, beam current, and relative ratio of the charge states of ions in the beam, providing the necessary information for calculation of the efficiencies of the plasma production and acceleration mechanisms. To determine the ion energies and charge state ratio of the beam, a traditional $E \times B$ probe and the EVADER probe were both placed on a 4 degree of freedom motion stage as shown by Fig. 2.11, with the traditional $E \times B$ probe sitting on top of the EVADER probe.



Figure 2.11: $E \times B$ and EVADER probes mounted to the 4DOF motion stage

During measurement the probes were held stationary 1.5 meters downstream from the face of the thruster, with the probe entrance hole in line with the center of the thruster. Alignment of the probes was accomplished by first moving the probes as close as possible to the thruster and then carefully measuring the horizontal and vertical distance to the thruster center, and adjusting the position of the motion stage based on these measurements.

The traditional $E \times B$ probe required only a Keithley 6517A electrometer and a Lambda GENH150-5 power supply. The power supply applies a bias to the suppressor of 20V, while the Keithley 6517A is used to bias the the plates in the transmission segment, and also to measure the current collected by the probe. The electrical schematic for the $E \times B$ probe is shown by Fig. 2.12. The voltage applied between the plates in the transmission segment is swept so as to filter the ions by velocity, and thus charge state.

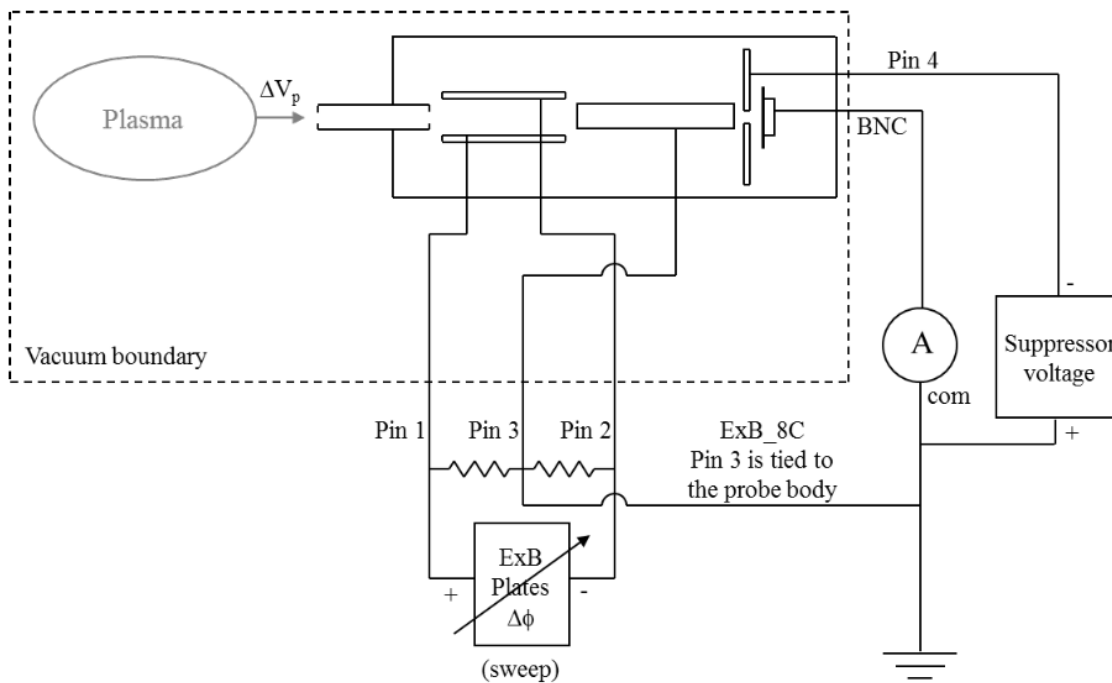


Figure 2.12: Circuit diagram for the $E \times B$, provided by Plasma Controls, LLC

The EVADER probe is capable of operation as either a traditional electrostatic analyzer (ESA) allowing measurement of the ion energy distribution, or as an ESA in combination with an $E \times B$

probe, allowing the measurement of ion charge state at selected energies per charge. Data were collected first with the EVADER operating as a standalone ESA. The procedure for data collection with an ESA described by Farnell et al. was used [29]. For all data presented in this thesis, the transmission energy of the ESA section was set to 375eV. By sweeping the voltage applied to the entrance of the ESA, with the E×B section of the EVADER disconnected, the EVADER provides only the ion energy distribution function trace. A voltage sweep from -400V to +100V was conducted using a Keithley 6517A and a program written by Shawn Farnell from Plasma Controls, LLC. The suppressor was biased to a constant 20V using a Lambda GENH150-5 power supply.

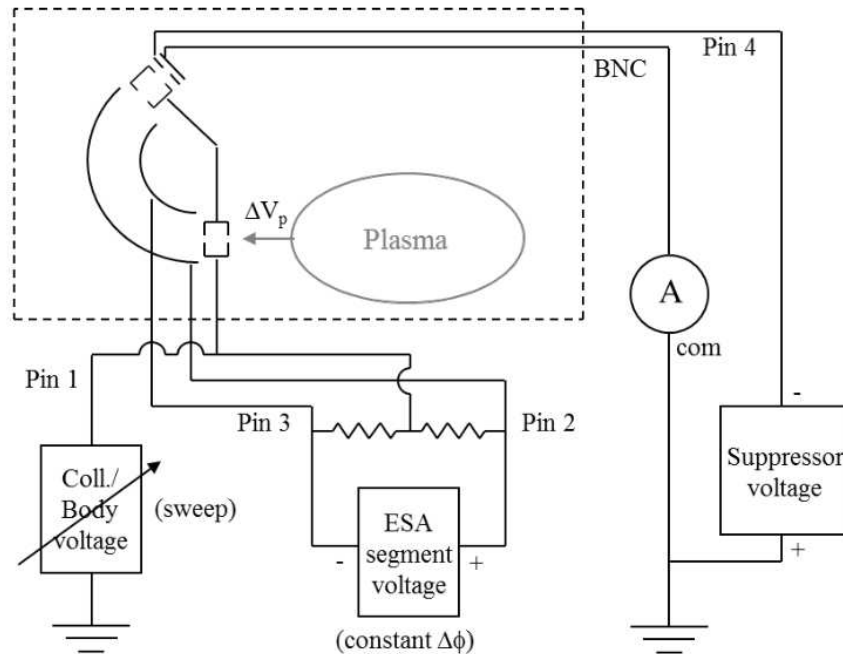


Figure 2.13: Circuit diagram for the ESA, provided by Plasma Controls, LLC

To gather ionization species ratios at selected energy levels, the E×B section of the EVADER probe was re-connected, and traces at selected energy levels were taken to determine the charge states of ions at specific energies per charge. The energy of the ions was selected by biasing the entrance of the EVADER probe to a constant voltage (rather than sweeping the voltage as in the ESA-only operation) using a Sorensen XG-600-1.4 power supply. The voltage on the E×B

section of the EVADER was then swept using the Keithley 6517A. The suppressor was biased to a constant 20V using a Lambda GENH150-5 power supply. The circuit diagram for the EVADER probe is shown in Fig. 2.14.

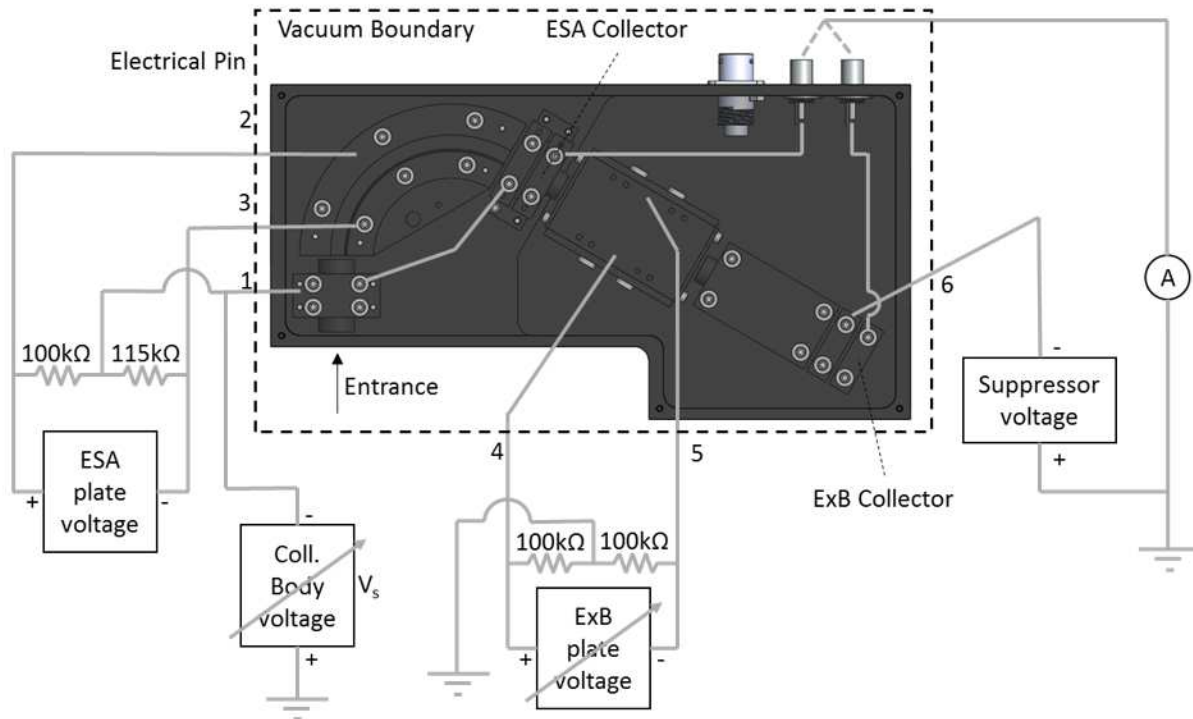


Figure 2.14: Circuit diagram for the EVADER probe, provided by Plasma Controls, LLC

A Faraday probe was mounted on a motion arm attached to the side of the thrust stand frame as shown in Fig. 2.15. The arm was connected to a stepper motor providing capability for a vertical arc sweep of 150 degrees at a radius of 29.75 inches from the face of the HET. The motor controlling the probe arm was shielded from the heat radiation from the plasma by several layers of thin steel, and the temperature was monitored by a thermocouple mounted to the outside of the motor.



Figure 2.15: Faraday probe and motion system

The Faraday probe was biased at -20 V relative to the cathode potential to repel electron current, and magnets were also attached to the body of the probe to further repel any electrons, first studied and reported in [28]. A close up of the probe with the magnets affixed to the guard ring is shown in Fig. 2.16. Motion of the arm, bias of the probe electrodes, and data acquisition were all controlled with a LabVIEW program created by Shawn Farnell at Plasma Controls, LLC.



Figure 2.16: The magnetically filtered Faraday probe used for this research

Chapter 3

Analysis Methods

Each of the diagnostic probes previously described is used to collect ion currents which are measured and recorded by the data acquisition system along with the voltage applied to the probe. The recorded currents must then be corrected and analyzed to produce meaningful plots showing the desired representation of the data, and the desired parameters must be calculated. The specific outcomes of these analyses are the beam current and plume divergence from Faraday probe data, the ion energy distribution function (IEDF) from the ESA, and the ionization species current fractions from the E×B probe, which are, in turn, used in calculating the utilization efficiencies. For this research, scripts were written in MATLAB and Visual Basic for Applications (VBA) to process, analyze, and produce plots of the data for each probe.

3.1 Faraday Probe Data Analysis

The Faraday probe collects ion current by traveling in an arc across the plume of the thruster, giving a current density measurement versus angle relative to the thruster axis. Due to space-constraints in the vacuum chamber, in this research effort the probe could only traverse to 60 degrees on one side of the thruster axis, but a polynomial fit is used to approximate the current, so this is not believed to affect the calculation of the beam current. The beam current is represented in mathematical format by Equation 3.1 and is calculated using numerical integration.

$$I_b = 2\pi R_{fp}^2 \int_0^{\pi/2} j(\theta) \sin\theta d\theta \quad (3.1)$$

The divergence angle, defined as the average axial velocity of the plume ions divided by their average total velocity is also calculated using numerical integration in accordance with Equation 3.2 [8], which gives the cosine of the divergence angle.

$$\cos\delta = \frac{2\pi R_{fp}^2 \int_0^{\pi/2} j(\theta) \cos\theta \sin\theta d\theta}{I_b} \quad (3.2)$$

The raw current data are first corrected for facility affects by subtracting the current collected at 90 degrees from all measurements, since the current at this angle should theoretically be zero. This method assumes the current due to the charge exchange and scattered ions is the same at all angles [9], but the method was determined to be satisfactory. A comparison of the raw trace and the corrected trace is shown in Fig. 3.1.

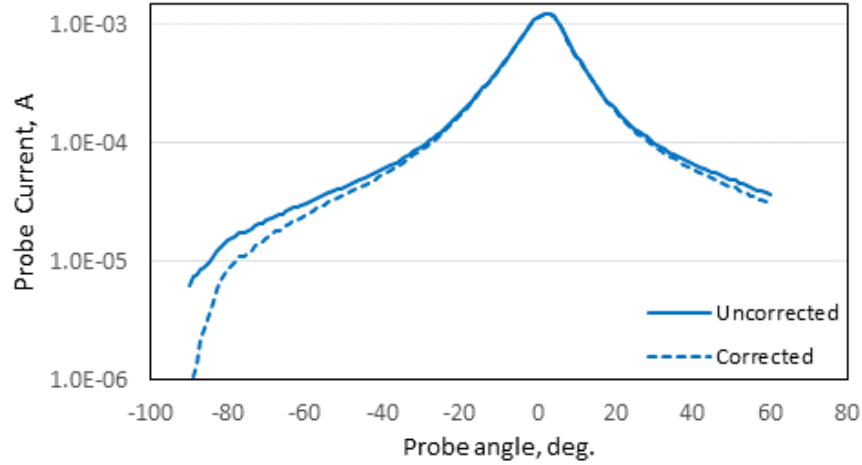


Figure 3.1: Raw and corrected Faraday probe trace at 300V, 4.75 mg/s with the center-mount cathode

The current data are then transformed to current density by dividing by the surface area of the probe collector. Next, the peak current density is found using the MATLAB *findpeaks()* function, and the data are shifted so that the peak corresponds to 0 degrees to account for misalignment of the probe. Next, a 6th order polynomial fit of the natural logarithm of the corrected data is found using the MATLAB *polyfit()* function. The script then numerically integrates the ion current on the hemispherical surface corresponding to the probe arc using a simple Riemann sum over 450 integration points.

3.2 Electrostatic Analyzer Data Analysis

The data acquired from the ESA consist of the current of ions collected at each of the voltages applied to the probe during the sweep. The ions only make it through the transmission segment of the probe and to the collector if they have the desired transmission energy, which is set by the voltage applied across the spherical plates in the transmission segment. Thus, for each voltage applied to the probe body in the sweep, the collected ions started in the plume at a potential energy equal to the transmission energy plus the applied probe voltage. For example, an ion that is collected by the probe with -100V applied to the probe body and a set transmission energy of 375 eV had a starting energy of 275 eV. By measuring the current collected at each voltage in the sweep, the ESA gives a distribution of the plume ions by their energy per charge. An example of the resulting plot, called an ion energy distribution function (IEDF) is shown by Fig. 3.2.

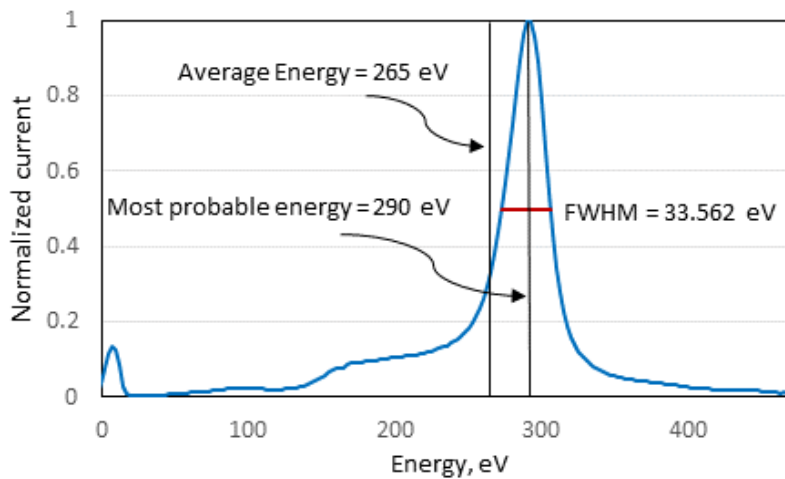


Figure 3.2: ESA trace at 300V, 4.75 mg/s with the center-mount cathode

Using the IEDF, the voltage utilization efficiency, described previously by Equation 1.9, can be calculated by dividing the voltage that the ions are accelerated through by the discharge voltage. There are several methods for determining the acceleration voltage based on the IEDF, but in much of the literature, the most probable energy, which is the energy corresponding to

the peak current, is used [8, 10]. In this effort, voltage utilization was calculated using both the most probable energy, and the average ion energy of the entire distribution. To analyze the ESA data, a VBA script was written to output these values. First, the transmission energy used is added to all of the applied voltages to determine the potential that the ion started at. Then, the peak current is found by looping through each data-point to determine the largest current value and it's corresponding energy-index. The average ion energy is calculated by summing the product of each energy value by its corresponding current value, and then dividing that sum by the total current. The full width at half max (FWHM) is also calculated by the script, and a normalized chart like the one shown in Fig. 3.2 is created automatically.

3.3 E×B Probe Data Analysis

The E×B probe filters ions by their velocity, which is a function of the ion's mass, charge state, and energy. In a monoenergetic beam consisting entirely of propellant atoms of the same mass, this corresponds to filtering by charge state and would produce distinctive, triangular peaks in current associated with each ionization species. However, the ions in a Hall thruster plume have a distribution of energies and thus the corresponding trace taken by an E×B probe often contains 'blending' (i.e. the current does not drop to zero) between the peaks as seen in the example trace shown by Fig. 3.3.

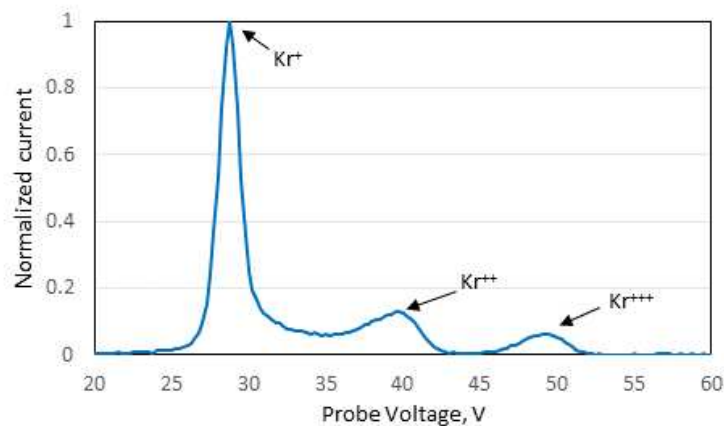


Figure 3.3: E×B probe trace at 300V, 4.75 mg/s with the center-mount cathode

Analysis of $E \times B$ data for Hall thruster plumes can be accomplished with several different methods, some of which detailed in [32, 33], but the general aim is to find the total current of each charge-state species of ions, and then calculate the current fraction for each species. For this work, the triangle method was chosen, in which the current of a particular charge species is approximated as the product of the peak current corresponding to that species and the half-width-at-half-max (HWHM). This method is meant to somewhat correct for the peak broadening associated with Hall thruster plumes [32]. To automate the analysis, a MATLAB script was created to analyze the data measured by the $E \times B$ probe. The script first corrects the data by subtracting the average of the last five data points (as these are assumed to be noise) from every other data point, effectively setting the noise-floor. The script then determines the location of the three peaks corresponding to singly, doubly, and triply charged Kr ions using the built-in MATLAB *findpeaks()* function. The HWHMs are then calculated using interpolation, and the total current approximation for each species is calculated by multiplying each peak by its corresponding HWHM, essentially approximating the peak as a triangle and using the area of that triangle as the representation of the species current. The current fractions for each species are then calculated by dividing the species current by the sum of the species currents (the sum of the three triangle areas), and the charge utilization and mass utilization efficiencies can then be calculated with Equations 1.10 and 1.11.

Chapter 4

Test Procedure and Results

4.1 Procedure

Over the course of this research effort, a standard operating procedure was developed for the operation and testing of the CSU Hall thruster. The heaterless cathode was ignited first, using a "gas burst" technique [13] with 600V applied between the cathode and keeper. Once ignited, the cathode was allowed to stabilize for several minutes, and then 4.25 mg/s Kr gas was supplied to the anode. The anode power supply was set to limits of 300V and 6.5A, and then power was output to the anode, igniting the thruster, which resulted in power supply operation at the current limit and anode voltage of about 50V. Next, the magnetic coil power supplies were turned on and current to each of the coils was slowly increased, building the magnetic field and the impedance of the plasma until the anode-to-cathode potential reached the 300V setting and the anode power supply switched into controlled voltage operation. At this point, the HET was deemed to be in "thruster" mode.

After ignition of the thruster, a warm-up period of 2 hours was observed to allow the thruster and thrust stand to reach thermal equilibrium so as to minimize thermal effects on thrust measurement. For each operating condition (a set of predetermined anode voltages and mass-flow rates) the discharge voltage and anode flow rate were first set. Anode voltages of 275V, 300V, and 325V were used, and anode mass-flow-rates were tested at each anode voltage ranging from 4.25 mg/s to 5.25 mg/s in increments of 0.25 mg/s. For nominal operation, the currents supplied to the magnetic circuit were then adjusted until the discharge current was minimized at a given operating condition.

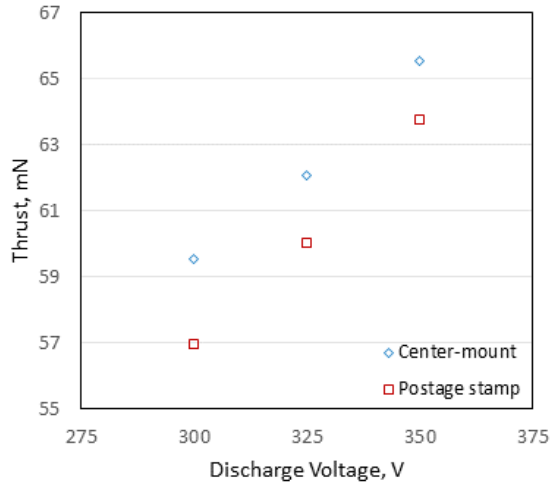
For the high performance mode of operation, the currents supplied to the coils were increased until a mode transition was visually noted by the change in plasma plume brightness. The effect of the coil currents after this transition was explored to determine the currents that

would give the highest thrust, and generally to see how sensitive the operation of the thruster in this mode was to changes in the magnetic field. It was determined that once in the high performance operation mode, 7A to the inner coil and 5-6A to the outer coil were generally found to be the best settings, but the operation was not greatly affected by changes to the coil currents as long as they were near these settings $\pm 0.5A$. The CSU Hall thruster was designed to have large margins for coil currents before saturation of the magnetic materials would occur. It also has large margins before the magnetic coils would fail due to temperature. These margins allowed us to examine the high performance mode of operation.

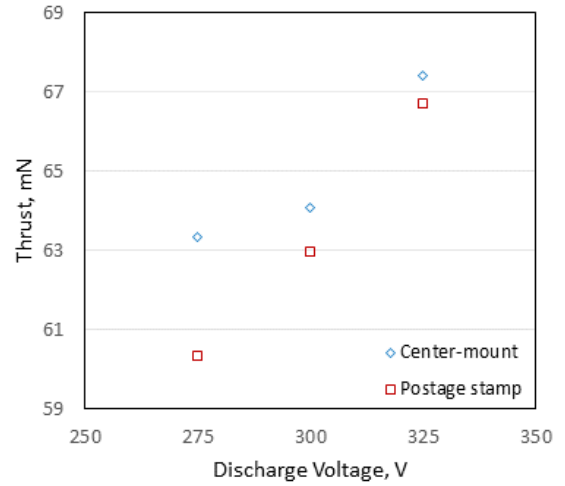
4.2 Test Results

4.2.1 Performance Comparison with Two Cathodes

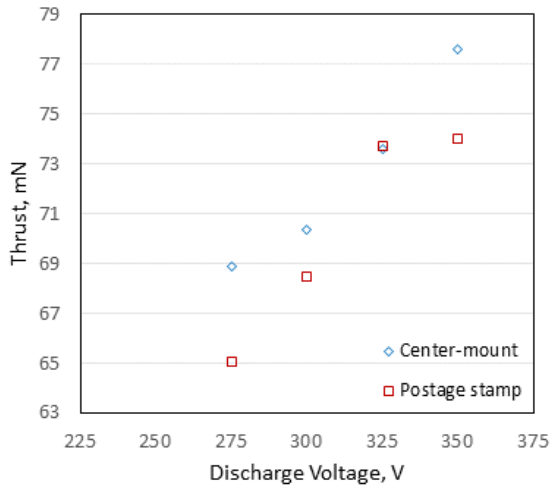
The first round of testing was performed with both cathodes in April 2019. At the time, the plasma diagnostic probes were not set up yet, so analysis focused on thrust measurement and performance characterization. Figure 4.1 contains plots of thrust as a function of discharge voltage for the first data-set, which was varied from 250 V to 350 V, at each of the five anode mass-flow rates. The thrust produced by the CSU Hall thruster fell between 59.6 and 85.0 ± 1.5 mN with the center-mount cathode, and between 57.0 and 85.4 ± 1.5 mN with the postage stamp cathode. The thrust increased with discharge voltage at each anode flow condition, and the center-mount cathode configuration produced higher thrust in all cases except for the conditions 4.75-5.25 mg/s at 325V. At all operating conditions except those three, the postage stamp cathode configuration is shown to result in 1-3 mN lower thrust compared to the center-mounted configuration. The average difference between thrust measurements at all discharge voltage and anode flow conditions was 2.0 mN (with the average difference being 2.4 mN in the cases where the center-mount outperformed the postage stamp, and the average difference being 0.4 mN in the few cases where the postage stamp outperformed the center-mount). It is noted that the estimated error in the thrust measurements is ± 1.5 mN, which is close to the difference between the two cathode configurations at many of the operating points.



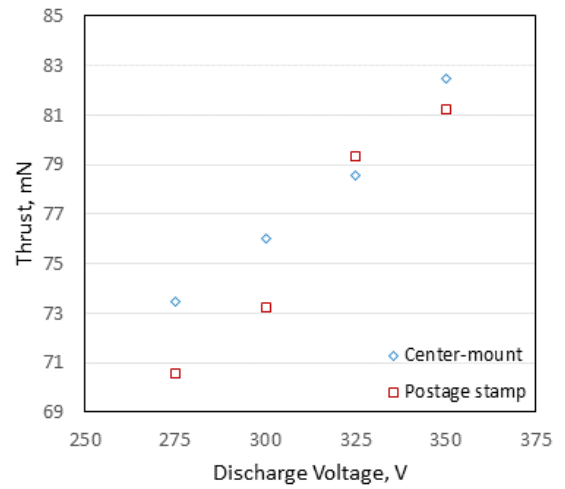
(a) 4.25 mg/s krypton



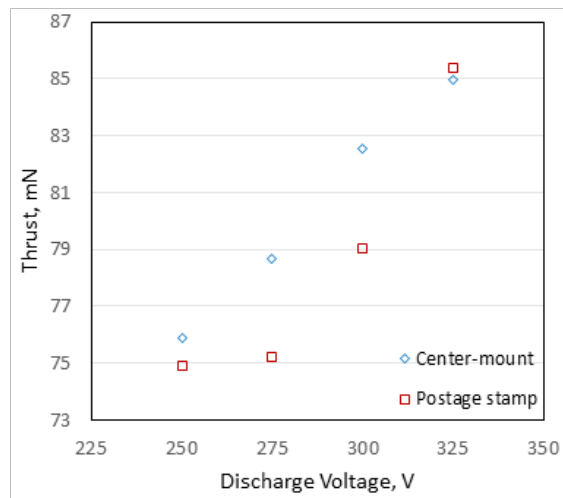
(b) 4.5 mg/s krypton



(c) 4.75 mg/s krypton



(d) 5.0 mg/s krypton

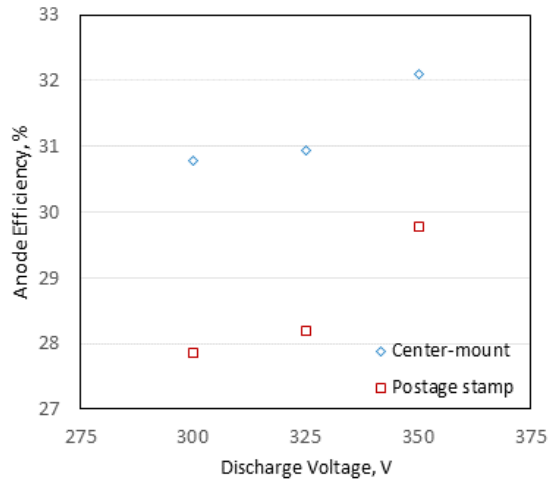


(e) 5.25 mg/s krypton

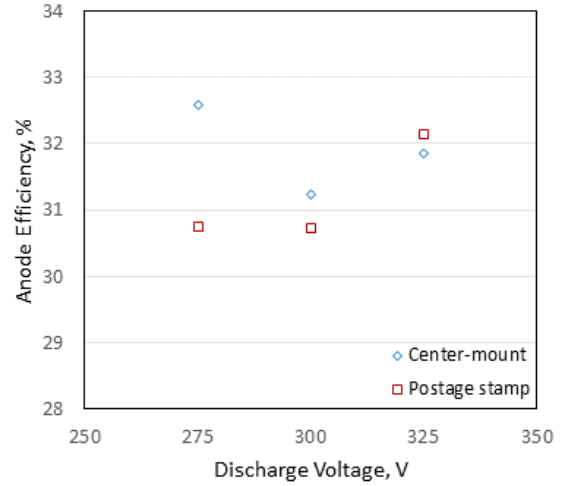
Figure 4.1: Thrust as a function of discharge voltage and anode mass flow-rate for the April 2019 data-set

The anode efficiency of the thruster ranged from 30.8% to 36.4% with the center-mount cathode, and from 27.9% to 37.2% with the postage stamp cathode. Plots of the anode efficiency as a function of discharge voltage, contained in Fig. 4.2, show a general trend of 0.5-3% lower efficiency for the postage stamp cathode, however, the postage stamp had higher efficiency at five of the eighteen operating conditions: 4.5-5.25 mg/s at 325V, and 5.25 mg/s at 250 V, and [5.25 mg/s, 325 V]. Although these data points suggest a possible advantageous discharge voltage for the postage stamp cathode at 325 V, this result could also be explained by non-ideal optimization of the electromagnets during the center-mounted cathode testing at that operational set-point and by uncertainty in the anode efficiency values that is roughly estimated to be $\pm 5\%$ of the calculated efficiency. The average difference between anode efficiency at a given discharge voltage was 1.71% (with an average difference of 1.98% in the cases where the center-mount cathode outperformed the postage stamp, and an average difference of 1.01% when the postage stamp outperformed the center-mount cathode). Interestingly, a dip in efficiency is observed at 300 V for many of the anode flow-rate conditions that were tested. In comparison, a flight model SPT-100 running on krypton propellant was shown by Nakles et al. [39] to have anode efficiency ranging from roughly 32% to 45% for discharge voltage varying from 250 V to 350 V and anode flow varying from 4.09 mg/s to 5.31 mg/s.

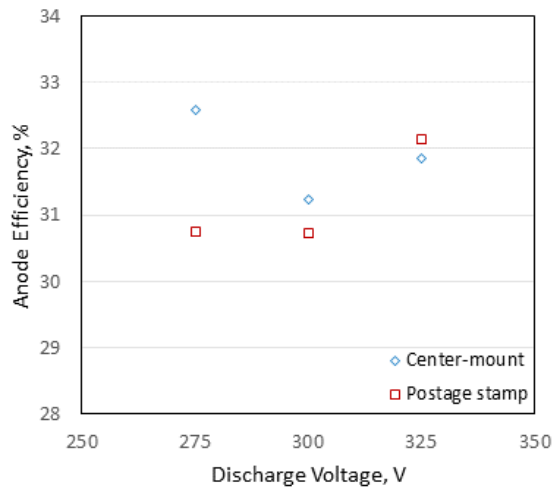
As expected, the anode specific impulse data, contained in Fig. 4.3, show a similar trend to the thrust data in Fig. 4.1, with only a few of the postage stamp data-points higher than the center-mount. The center-mount configuration produced anode I_{sp} ranging from 1430 to 1684 seconds, and the postage stamp configuration produced anode I_{sp} ranging from 1368 to 1658 seconds with an estimated 3% uncertainty. In addition, similar to thrust and as expected, the anode I_{sp} increased with increasing discharge voltage. The center-mount cathode produced higher anode I_{sp} in all cases except 4.75-5.25 mg/s at 325 V. The average difference in anode specific impulse at a given discharge voltage and anode-mass-flow rate was 44 sec (with the average difference being 51 sec when the center-mount configuration outperformed and the average difference being 8.6 sec when the postage stamp configuration outperformed).



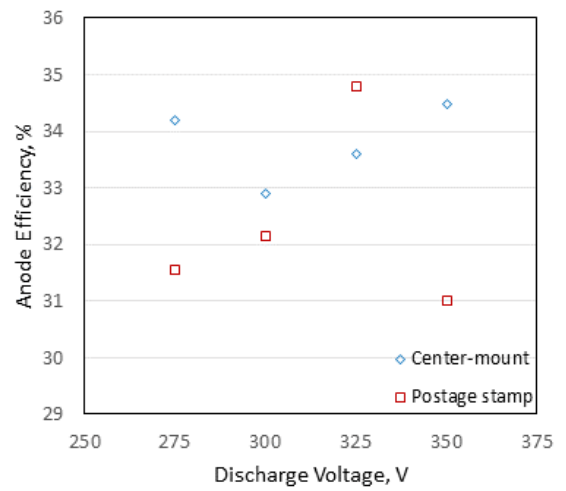
(a) 4.25 mg/s krypton



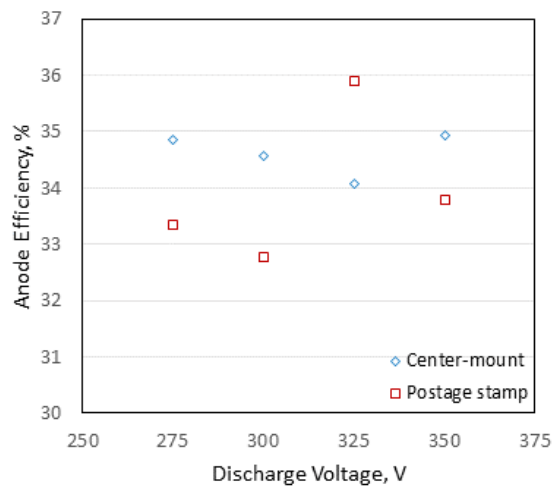
(b) 4.5 mg/s krypton



(c) 4.75 mg/s krypton

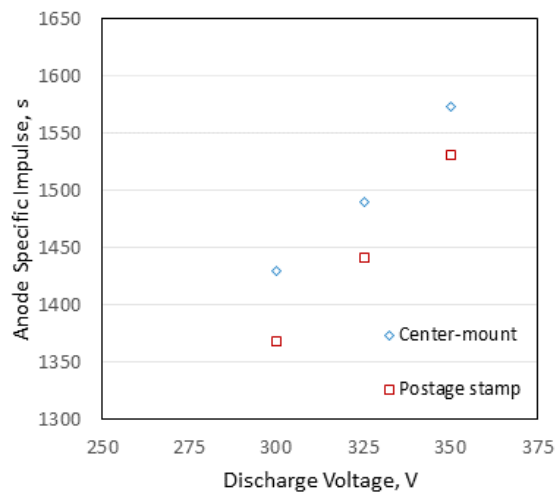


(d) 5.0 mg/s krypton

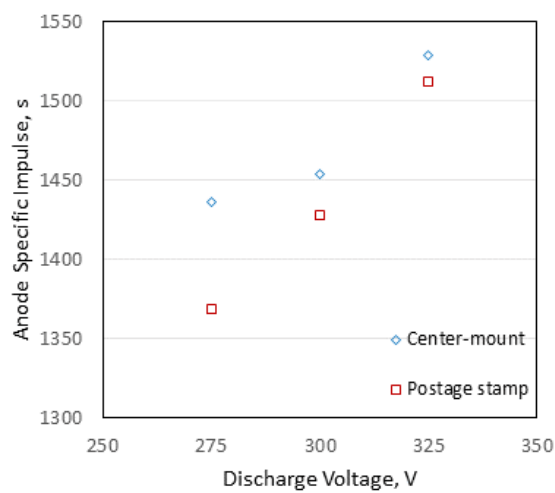


(e) 5.25 mg/s krypton

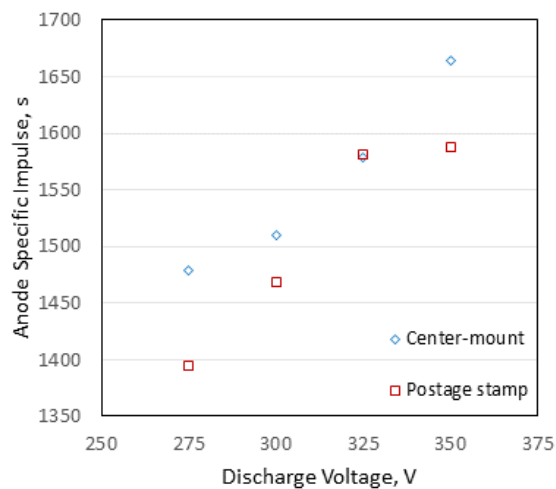
Figure 4.2: Anode efficiency as a function of discharge voltage and anode mass flow-rate for the April 2019 data-set



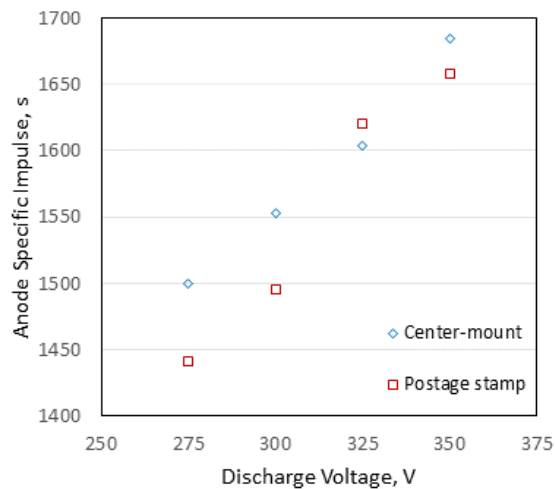
(a) 4.25 mg/s krypton



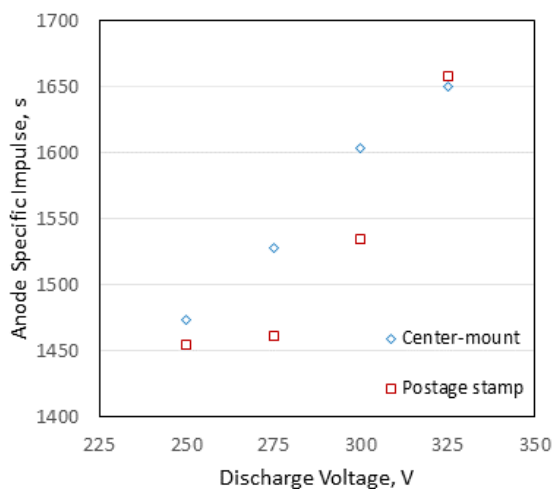
(b) 4.5 mg/s krypton



(c) 4.75 mg/s krypton



(d) 5.0 mg/s krypton



(e) 5.25 mg/s krypton

Figure 4.3: Anode specific impulse as a function of discharge voltage and anode mass flow-rate for the April 2019 data-set

The full data-sets for the April 2019 test with the center-mounted and postage stamp cathodes are shown in Tables 4.1 and 4.2.

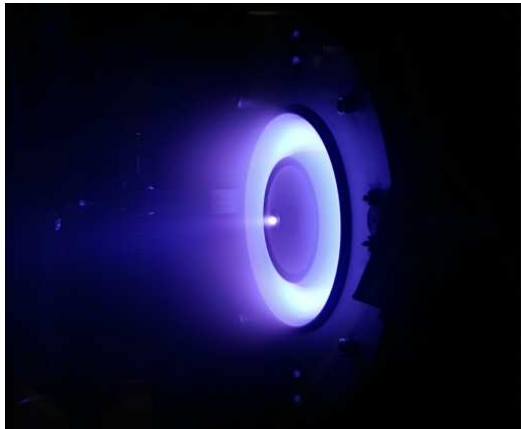
Table 4.1: April 2019 test using the center-mounted cathode

V_{anode}	\dot{m}_{anode}	P_{anode}	T	$I_{sp, anode}$	η_{anode}
(V)	(mg/s)	(W)	(mN)	(s)	(%)
250	5.25	1504	75.9	1474	36.4
275	4.50	1369	63.3	1436	32.6
275	4.75	1460	68.9	1479	34.2
275	5.00	1549	73.5	1500	34.9
275	5.25	1649	78.7	1529	35.8
300	4.25	1356	59.6	1430	30.8
300	4.50	1463	64.1	1454	31.2
300	4.75	1584	70.4	1510	32.9
300	5.00	1675	76.0	1553	34.6
300	5.25	1794	82.6	1604	36.2
325	4.25	1466	62.1	1490	30.9
325	4.50	1587	67.4	1529	31.9
325	4.75	1696	73.6	1579	33.6
325	5.00	1813	78.6	1604	34.1
325	5.25	1939	85.0	1651	35.5
350	4.25	1577	65.6	1574	32.1
350	4.75	1836	77.6	1665	34.5
350	5.00	1950	82.5	1684	34.9

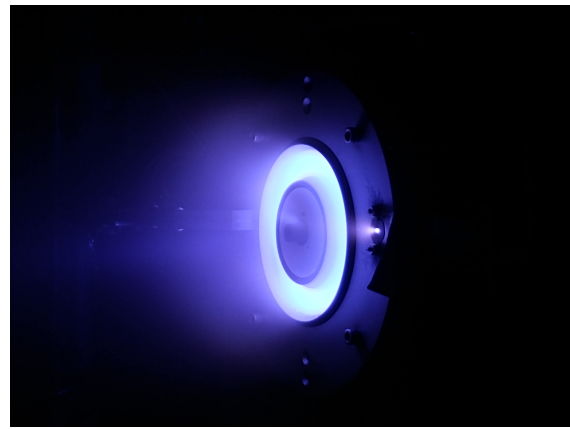
Table 4.2: April 2019 test using the postage stamp cathode

V_{anode}	\dot{m}_{anode}	P_{anode}	T	$I_{sp, anode}$	η_{anode}
(V)	(mg/s)	(W)	(mN)	(s)	(%)
250	5.25	1464	74.9	1455	36.5
275	4.50	1317	60.3	1369	30.7
275	4.75	1410	65.0	1395	31.5
275	5.00	1495	70.6	1441	33.3
275	5.25	1607	75.2	1461	33.5
300	4.25	1372	57.0	1368	27.9
300	4.50	1436	63.0	1429	30.7
300	4.75	1534	68.4	1469	32.1
300	5.00	1639	73.3	1496	32.8
300	5.25	1735	79.0	1535	34.3
325	4.25	1505	60.0	1441	28.2
325	4.50	1539	66.7	1513	32.2
325	4.75	1643	73.7	1582	34.8
325	5.00	1756	79.3	1620	35.9
325	5.25	1866	85.4	1658	37.2
350	4.25	1609	63.8	1532	29.8
350	4.75	1859	74.0	1588	31.0
350	5.00	1953	81.2	1658	33.8

A second comprehensive set of data was collected in February of 2020 after a redesign and fabrication of the center mounted cathode, a second rebuild of the magnetic coils, and the setup of the full suite of plasma diagnostic probes. Additionally, during this test campaign the high performance mode was discovered and investigated. Pictures of the thruster running with both cathodes are shown in Fig. 4.4 below.



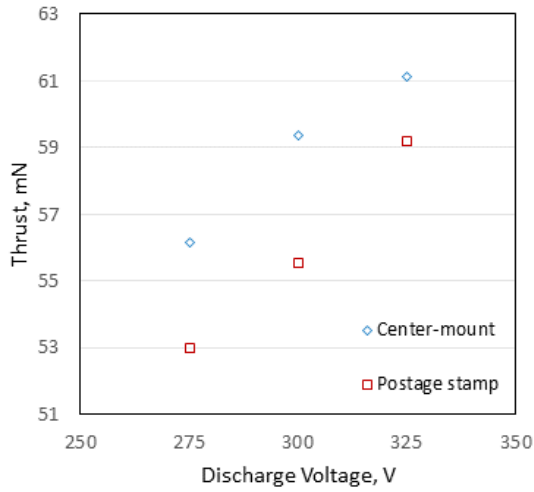
(a) Operation with the center mounted cathode



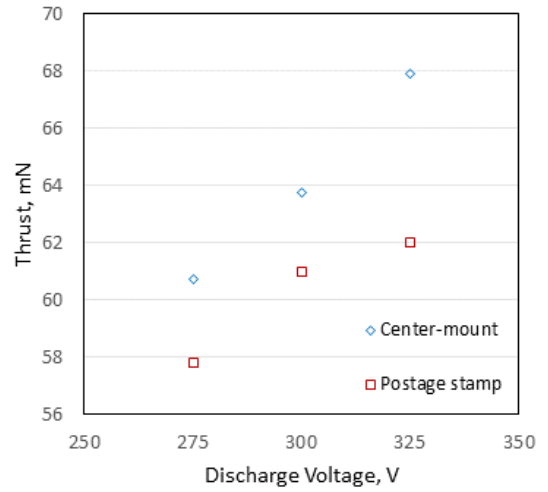
(b) Operation with the Postage stamp cathode

Figure 4.4: CSU Hall thruster operating during the February 2020 test campaign

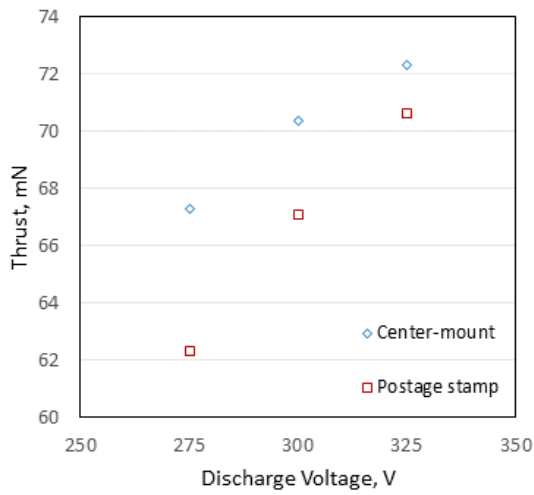
The thrust produced by the Hall thruster in the second test campaign fell between 56.1 mN and 84.9 mN \pm 1.5 mN with the center-mount cathode, and between 53.0 mN and 79.7 mN \pm 1.5 mN with the postage stamp cathode. The thrust again increased with discharge voltage at each anode flow condition, and in this test campaign, the center-mount cathode configuration produced higher thrust in all cases. The average difference between thrust measurements at all discharge voltage and anode flow conditions was 4.46 mN. In most cases, the difference in thrust was not within the error, leading to the conclusion that use of the center mounted cathode generally results in higher thrust production at any given discharge voltage and anode mass-flow-rate. Thrust is plotted against discharge voltage for each anode mass-flow rate in Fig. 4.5



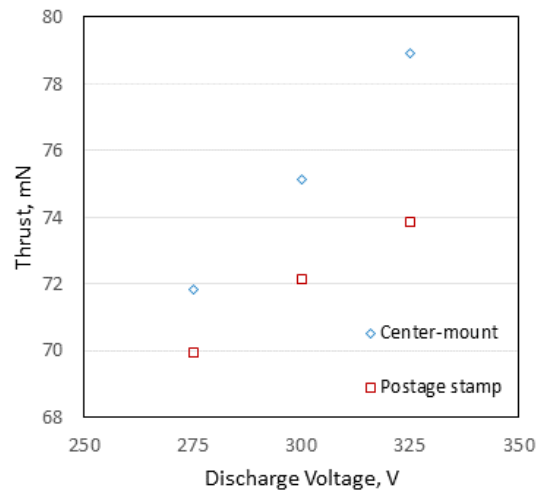
(a) 4.25 mg/s krypton



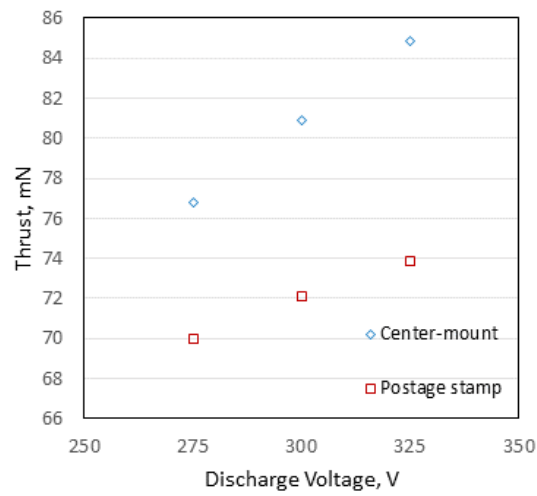
(b) 4.5 mg/s krypton



(c) 4.75 mg/s krypton



(d) 5.0 mg/s krypton

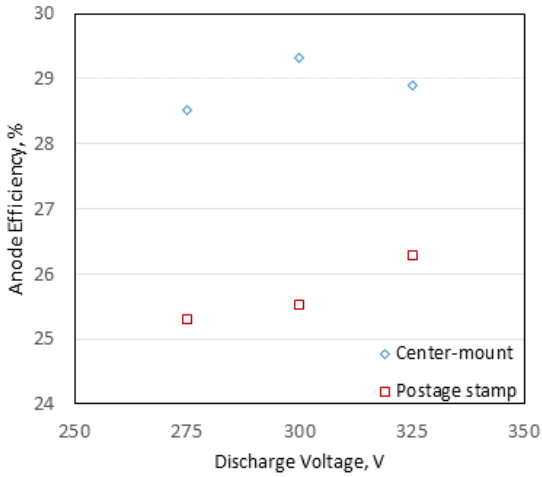


(e) 5.25 mg/s krypton

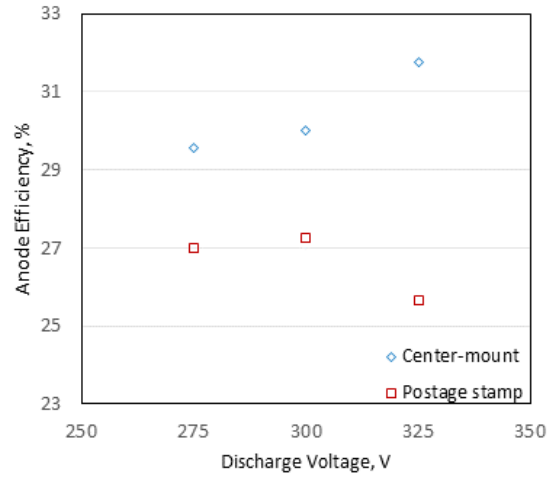
Figure 4.5: Thrust as a function of discharge voltage and anode mass flow-rate for the February 2020 data-set

The anode efficiency of the thruster during the February 2020 test campaign ranged from 28.5% to 34.8% with the center-mount cathode, and from 25.3% to 33.6% with the postage stamp cathode. Plots of the anode efficiency as a function of discharge voltage, contained in Fig. 4.6, show a general trend of lower efficiency for the postage stamp cathode throughout all cases. In several cases, the efficiency at 325V with the postage stamp cathode was lower than the efficiency at 300V, departing from the trend generally seen of increasing efficiency with increasing discharge voltage. This result could be explained by non-ideal optimization of the electromagnets and by uncertainty in the anode efficiency values that is roughly estimated to be 5% of the calculated value. The average difference between the anode efficiency at any given discharge voltage and anode mass-flow-rate was 3 percentage points.

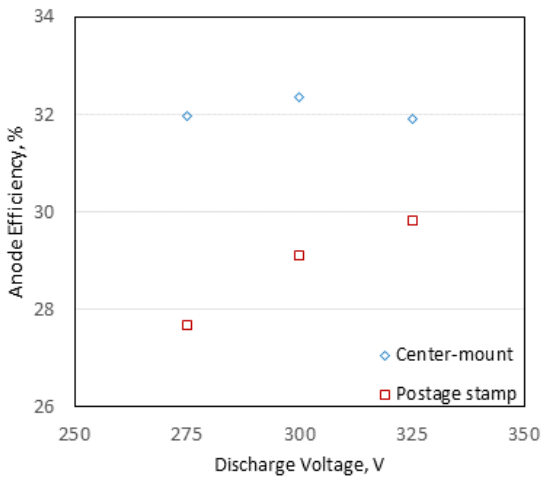
The anode specific impulse data for the second test campaign are contained in Fig. 4.7. The center-mount configuration produced anode I_{sp} ranging from 1348 seconds to 1648 seconds, and the postage stamp configuration produced anode I_{sp} ranging from 1272 seconds to 1547 seconds. Similar to thrust, the anode I_{sp} increased with increasing discharge voltage and increasing anode mass-flow-rate. The center-mount cathode produced higher anode I_{sp} in all cases. The average difference in anode specific impulse at a given discharge voltage and anode-mass-flow rate was 74 seconds. The uncertainty in the anode specific impulse, based on the thrust measurement uncertainty, is estimated to be 3% of the calculated value.



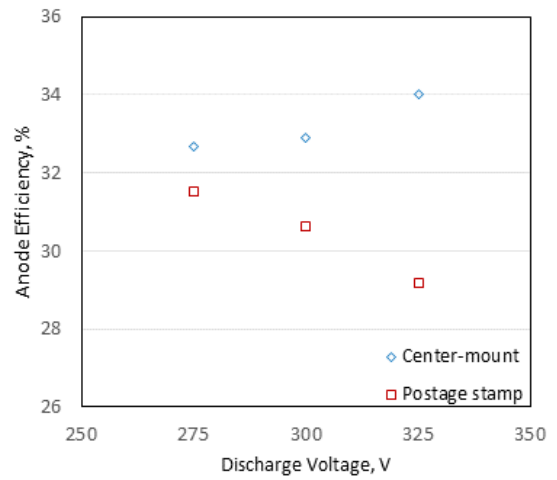
(a) 4.25 mg/s krypton



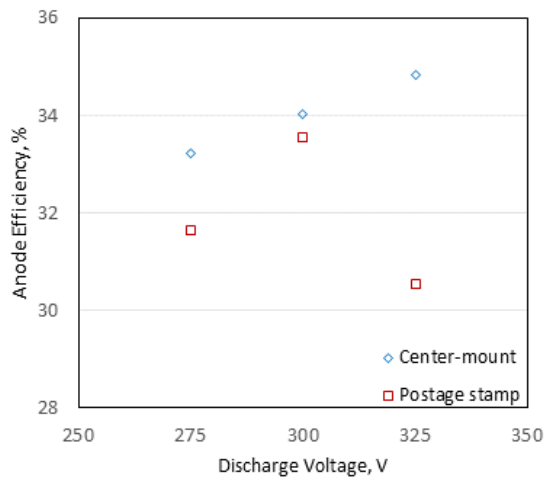
(b) 4.5 mg/s krypton



(c) 4.75 mg/s krypton

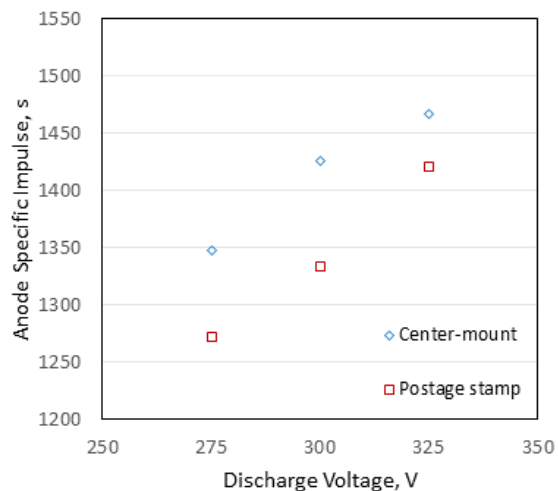


(d) 5.0 mg/s krypton

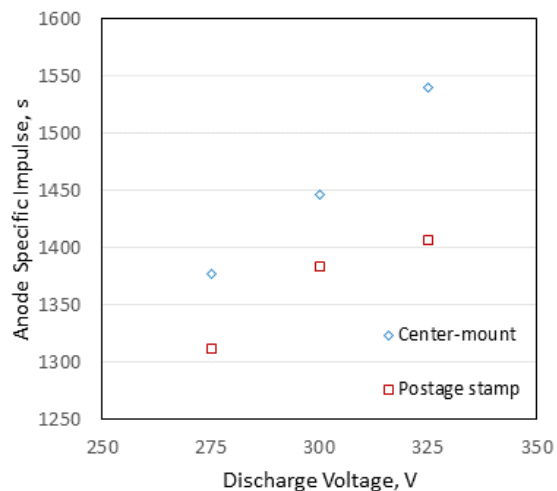


(e) 5.25 mg/s krypton

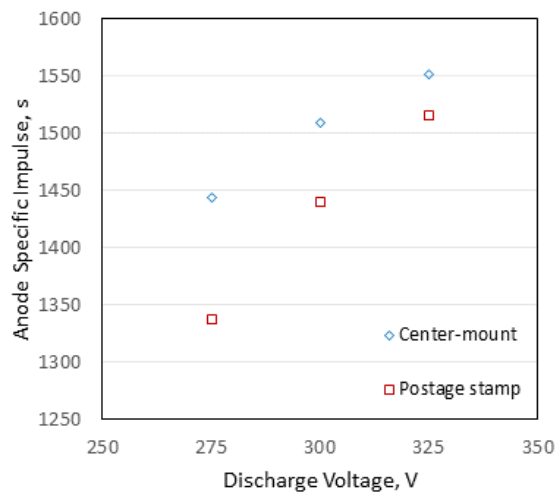
Figure 4.6: Anode efficiency as a function of discharge voltage and anode mass flow-rate for the February 2020 data-set



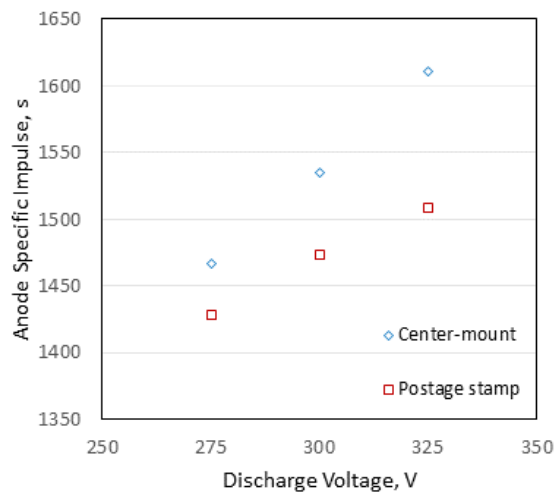
(a) 4.25 mg/s krypton



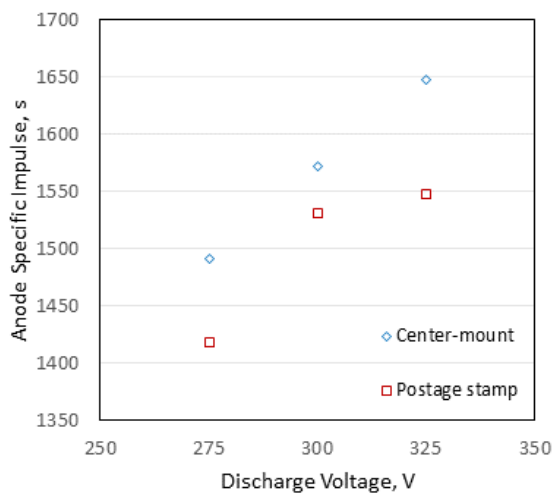
(b) 4.5 mg/s krypton



(c) 4.75 mg/s krypton



(d) 5.0 mg/s krypton



(e) 5.25 mg/s krypton

Figure 4.7: Anode specific impulse as a function of discharge voltage and anode mass flow-rate for the February 2020 data-set

Data collected with the suite of diagnostic probes were used to calculate the utilization efficiencies, the equations for which were explained in Chapter 2. The current traces collected by the ESA, ExB, and Faraday probes can give insights into the differences between operating conditions, so examples of each at the 300V, 4.75 mg/s operating point are shown in Figs. 4.8, 4.10, and 4.12. As shown by the ESA traces, Fig. 4.8, the most probable energy of the plume ions when using the postage stamp cathode configuration is several electron-volts lower than when using the center-mount cathode. The postage stamp configuration also contains a slightly larger high-energy shoulder, and a larger presence of charge-exchange ions at slightly higher energy (measured relative to ground potential). The charge exchange data suggest that the postage stamp might be less effective at keeping the far-field plume plasma potential to low values.

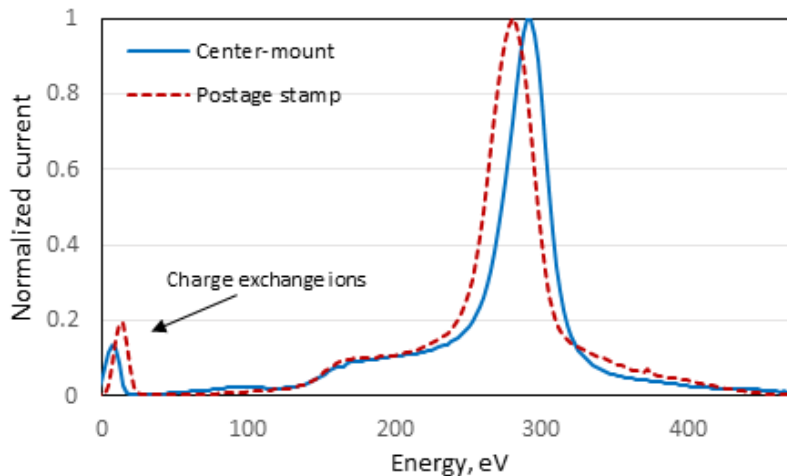
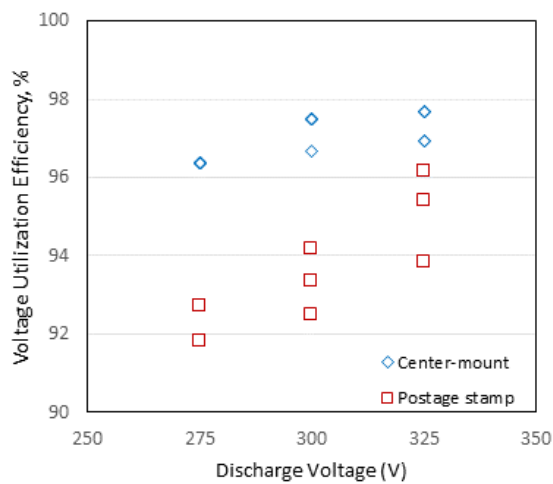


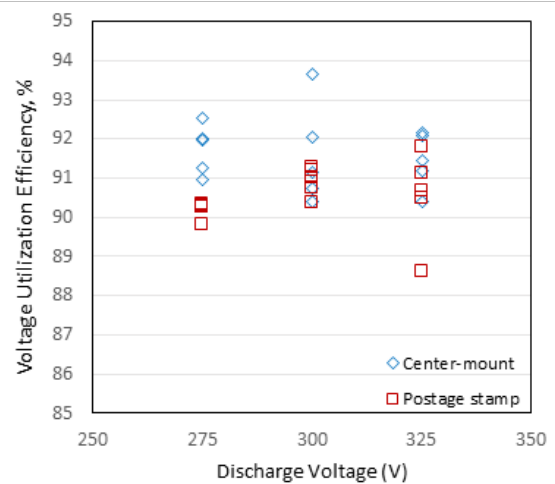
Figure 4.8: ESA traces at 300V, 4.75 mg/s with the center-mount and postage stamp cathodes

Lower most probable beam ion energy and average beam ion energy with the postage stamp configuration was a general trend at all operating conditions, resulting in lower voltage utilization efficiencies for the postage stamp configuration in every case, as shown in Fig. 4.9. Using the most probable energy for the calculation, voltage utilization efficiency ranged from 96.4% to 97.7% with the center mounted cathode, and from 91.8% to 96.2% with the postage stamp cathode. Using the average ion energy for calculation of voltage utilization, it ranged from 90.4%

to 93.7% with the center-mount, and from 88.6% to 91.8% with the postage stamp. These data indicate that the thruster does not accelerate ions as efficiently when operating with the pole-piece-mounted postage stamp cathode than with the center-mounted cathode. When calculated with the most probable ion energy, voltage utilization efficiency showed a general trend of increasing efficiency with increasing discharge voltage for both configurations. However, when calculated with the average ion energy, voltage utilization showed a somewhat decreasing trend in the center-mount configuration indicating a larger amount of lower-than-most-probable-energy ions at higher voltage operating points.



(a) Calculated with the most probable ion energy



(b) Calculated with the average ion energy

Figure 4.9: Voltage utilization efficiency calculated with the most probable energy and average energy vs. discharge voltage for the HET with the center-mount and postage stamp cathodes

The plot of the Faraday probe traces shown in Fig. 4.10 shows that the postage stamp configuration produced a slightly lower peak current density at the center of the plume, but also a slightly higher current density in the left 'wing', which resulted in a higher total beam current with the postage stamp.

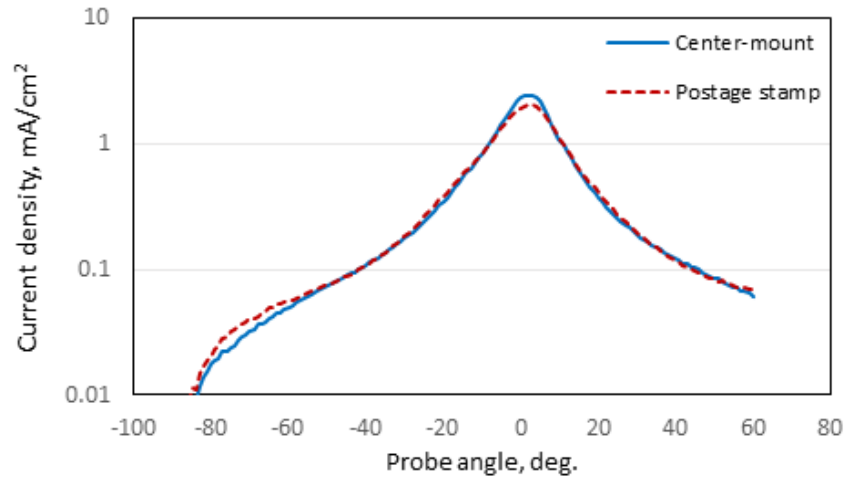
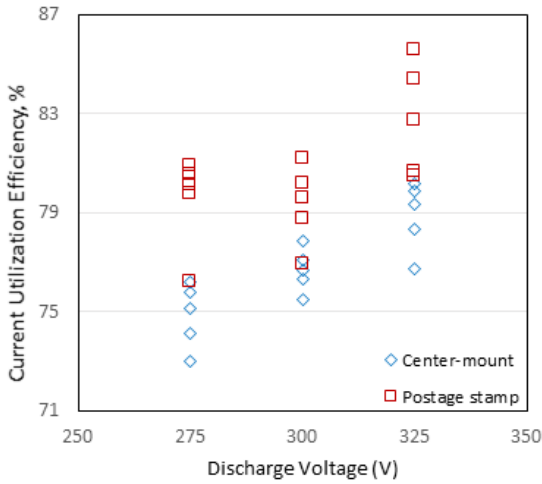
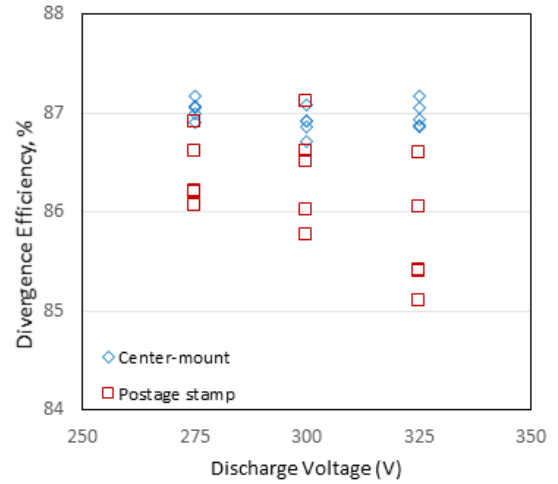


Figure 4.10: Faraday probe traces at 300V, 4.75 mg/s with the center-mount and postage stamp cathodes

This was the general trend in all operating points, leading to higher current utilization efficiencies for the postage stamp configuration. However, the higher current density in the wings means that the plume is more divergent, which is reflected in the general trend of lower divergence efficiency for the postage stamp. Current utilization efficiency ranged from 73.0% to 80.2% with the center-mounted cathode, and from 76.2% to 85.6% with the postage stamp. Divergence efficiency ranged from 86.7% to 87.2% with the center-mounted cathode, and from 85.1% to 87.1% with the postage stamp cathode. Current utilization efficiency typically increased with increasing discharge voltage, while divergence efficiency showed no strong trend in the center-mount data, but a decreasing trend with the postage stamp cathode, suggesting that higher voltage operating points cause higher beam divergence.



(a) Current utilization



(b) Divergence efficiency

Figure 4.11: Current utilization and divergence efficiencies vs. discharge voltage for the HET with the center-mount and postage stamp cathodes

Comparison of the ExB probe traces at the sample operating point, as seen in Fig. 4.12, show that a larger amount of doubly and triply charged ions were created when using the postage stamp cathode. This results in a lower charge utilization efficiency for the thruster in the postage stamp configuration. The leftward shift of the postage stamp trace is caused by the lower average ion energy that was previously shown in the ESA trace comparison.

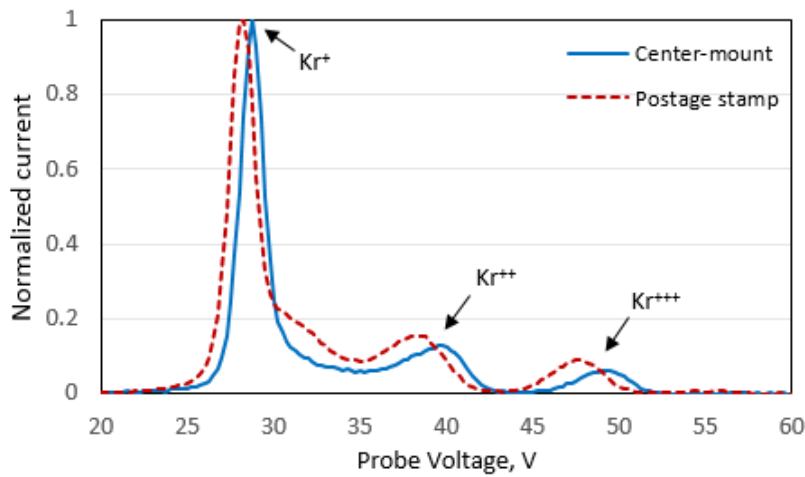


Figure 4.12: ESA traces at 300V, 4.75 mg/s with the center-mount and postage stamp cathodes

Charge and mass utilization efficiencies are shown in Fig. 4.13. Operation of the thruster using the center-mounted cathode resulted in charge utilization efficiencies ranging from 96.2% to 97.7%, and operation with the postage stamp cathode produced charge utilization efficiencies ranging from 96.5% to 97.6%. The average charge utilization efficiencies at each discharge voltage were 96.8%, 97.2%, and 97.3% respectively for the center-mount cathode configuration, and 97.0%, 97.0%, and 97.2% for the postage stamp cathode configuration. This indicates that the two configurations were very similarly efficient in ionization of the propellant. Furthermore, there does not seem to be a strong trend between discharge voltage and charge utilization.

Mass utilization efficiency ranged from 48.2% to 56.5% for the center-mounted cathode configuration and from 49.3% to 60.1% with the postage stamp cathode configuration. The postage stamp configuration outperformed in many of the cases, especially at the 325 V discharge conditions. This is due to the postage stamp having higher beam currents as discussed previously, while maintaining similar species current fractions to the center-mount configuration. There seems to be a strong increasing trend between mass utilization efficiency and discharge voltage, which is expected because of the general trend of increasing beam current with increasing discharge voltage.

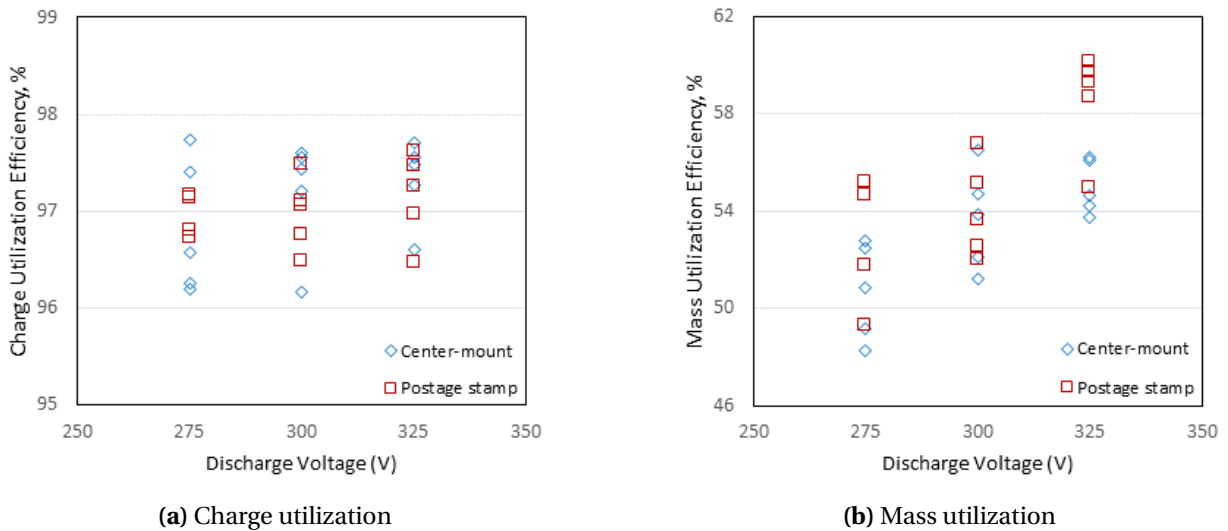
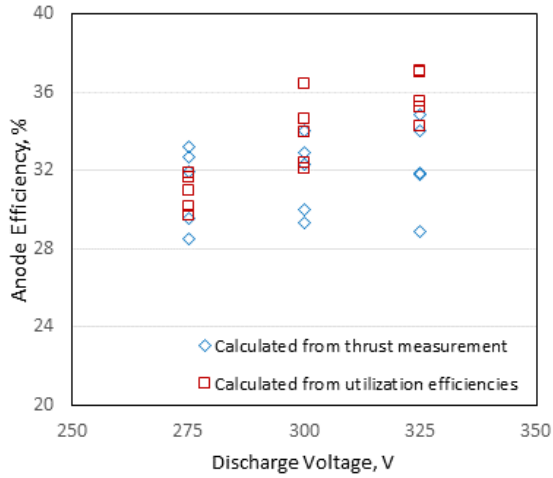
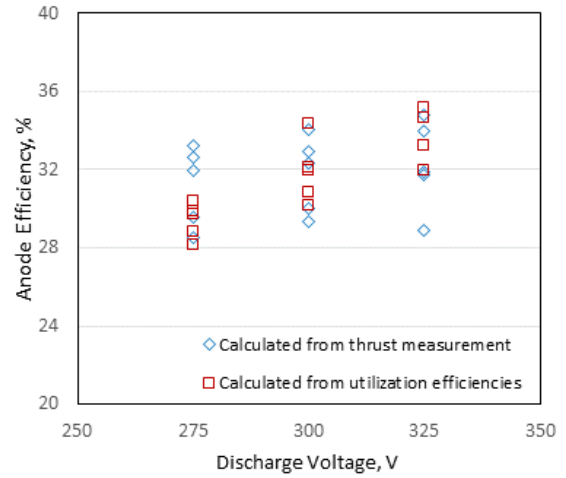


Figure 4.13: Charge and mass utilization efficiencies vs. discharge voltage for the HET with the center-mount and postage stamp cathodes

Figures 4.14 and 4.15 show, for each cathode, the anode efficiency calculated using Equation 1.6 and the recorded thrust measurement, flow rate, and power (thrust-derived), in comparison with the anode efficiency calculated using Equation 1.12 and the utilization efficiencies calculated from the diagnostic probe data (probe-derived). Figures 4.14a and 4.15a show the probe-derived anode efficiency calculated when using the most probable ion energy in calculating the voltage utilization efficiency, while Figures 4.14b and 4.15b show the probe-derived anode efficiency calculated when the average ion energy was used to calculate the voltage utilization efficiency. The lower voltage utilization efficiencies calculated using the average ion energy resulted in lower probe-derived efficiencies that matched more closely with the thrust-derived anode efficiency in both the center-mount and postage stamp cases, suggesting that the average ion energy may be a more accurate way to calculate the voltage utilization efficiency. A full uncertainty analysis was not conducted for the probe data and corresponding utilization efficiencies, but based on the analysis in [8], the uncertainty in the probe-derived anode efficiency is ~10% of the calculated value. Keeping the uncertainties in mind, the thrust-derived and probe-derived anode efficiencies are very much in line with each other in all cases with the center-mount cathode, and at 275V and 300V with the postage stamp. At 325V, the probe-derived anode efficiency is higher, and outside of the uncertainty range. This is a result of the high beam current calculated from the Faraday probe data at that discharge voltage during operation with the postage stamp, which resulted in high current and mass utilization efficiency. There is much less uncertainty involved with the thrust measurement, so we believe this discrepancy in the probe-derived efficiency is likely due to some error during the Faraday probe data collection at 325V with the postage stamp, potentially related to charge exchange ion collection. The filtered Faraday probe could have been biased in a way to repel charge exchange ions, but this was not done for this effort. Future work should be aimed at repeating these measurements to further investigate the discrepancy, as lab closure in the spring of 2020 due to the COVID-19 pandemic prevented further investigation for the time being.

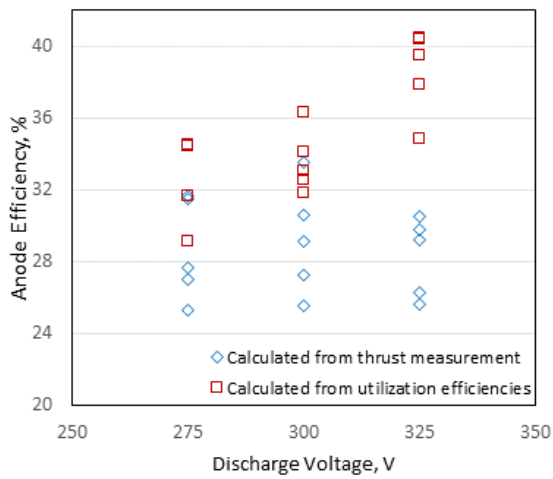


(a) Most probable ion energy used for η_v

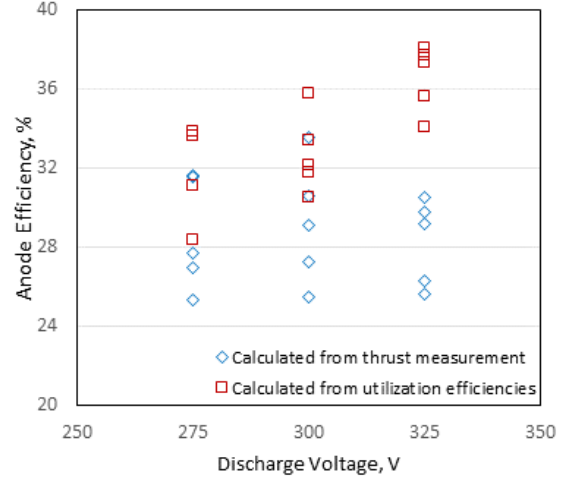


(b) Average ion energy used for η_v

Figure 4.14: Anode efficiency vs. discharge voltage calculated using the thrust measurement, and the utilization efficiencies with the center-mount cathode



(a) Most probable ion energy for η_v calculation



(b) Using average ion energy for η_v calculation

Figure 4.15: Anode efficiency vs. discharge voltage calculated using the thrust measurement, and the utilization efficiencies with the postage stamp cathode

The full data sets for the February 2020 test of the center-mounted and postage stamp cathodes are shown below in Tables 4.3 and 4.4, respectively.

Table 4.3: February 2020 test using the center-mounted cathode

V_{anode}	\dot{m}_{anode}	P_{anode}	T	$I_{sp,anode}$	η_{anode}	η_b	η_a	η_m	$\eta_{v,avg}$	$\eta_{v,mp}$	η_d	η_{aavg}	η_{amp}
(V)	(mg/s)	(W)	(mN)	(s)	(%)	(%)	(%)	(%)	(%)	(%)	(%)	(%)	(%)
275	4.25	1301	56.1	1348	28.5	73.0	97.7	52.9	91.0	96.4	87.1	29.9	31.6
275	4.50	1389	60.8	1378	29.6	74.1	97.4	52.5	92.0	96.4	87.2	30.4	31.9
275	4.75	1491	67.3	1444	32.0	76.2	96.2	48.3	91.2	96.4	87.0	28.1	29.7
275	5.00	1581	71.8	1467	32.7	75.8	96.2	49.3	92.0	96.4	87.1	28.8	30.2
275	5.25	1691	76.8	1492	33.2	75.1	96.6	50.9	92.5	96.4	86.9	29.7	30.9
300	4.25	1416	59.4	1426	29.3	75.5	97.4	52.1	90.8	97.5	86.7	30.2	32.4
300	4.50	1506	63.8	1446	30.0	76.3	97.6	54.8	90.4	97.5	86.9	32.1	34.6
300	4.75	1611	70.4	1510	32.3	77.1	97.2	53.9	91.1	96.7	86.9	32.0	33.9
300	5.00	1719	75.2	1535	32.9	77.9	97.6	56.6	92.1	97.5	86.9	34.4	36.4
300	5.25	1833	80.9	1572	34.0	76.7	96.2	51.3	93.7	97.5	87.1	30.8	32.1
325	4.25	1521	61.1	1467	28.9	76.7	97.7	54.3	90.4	96.9	86.9	32.0	34.3
325	4.50	1615	67.9	1540	31.8	78.3	97.6	54.7	91.4	97.7	87.1	33.3	35.5
325	4.75	1726	72.3	1552	31.9	79.9	97.5	56.1	91.2	97.7	86.9	34.6	37.1
325	5.00	1833	78.9	1611	34.0	80.2	97.3	56.3	92.1	96.9	86.9	35.1	37.0
325	5.25	1970	84.9	1648	34.8	79.3	96.6	53.9	92.2	97.7	87.2	33.2	35.2

Table 4.4: February 2020 test using the postage stamp cathode

V_{anode}	\dot{m}_{anode}	P_{anode}	T	$I_{sp,anode}$	η_{anode}	η_b	η_a	η_m	$\eta_{v,avg}$	$\eta_{v,mp}$	η_d	η_{aavg}	η_{amp}
(V)	(mg/s)	(W)	(mN)	(s)	(%)	(%)	(%)	(%)	(%)	(%)	(%)	(%)	(%)
275	4.25	1306	53.0	1272	25.3	76.2	96.8	49.4	90.3	92.7	86.2	28.4	29.1
275	4.50	1378	57.8	1311	27.0	79.8	96.7	51.8	90.3	91.8	86.2	31.1	31.6
275	4.75	1477	62.3	1338	27.7	80.5	97.1	55.3	90.3	92.7	86.1	33.6	34.5
275	5.00	1554	70.0	1428	31.5	80.1	N/A	N/A	89.8	91.8	86.6	N/A	N/A
275	5.25	1606	73.0	1419	31.6	80.9	97.2	54.9	90.3	91.8	86.9	33.9	34.4
300	4.25	1422	55.5	1333	25.5	76.9	97.1	52.6	90.4	94.2	86.0	30.5	31.8
300	4.50	1518	61.0	1384	27.3	79.6	97.1	55.2	91.3	93.3	85.8	33.4	34.1
300	4.75	1629	67.1	1440	29.1	78.8	96.8	53.7	90.7	93.3	86.5	32.1	33.0
300	5.00	1701	72.1	1473	30.6	80.2	96.5	52.1	91.0	93.3	86.6	31.7	32.6
300	5.25	1764	78.8	1531	33.6	81.2	97.5	56.9	91.2	92.5	87.1	35.8	36.3
325	4.25	1570	59.2	1421	26.3	80.5	97.6	58.7	90.5	96.2	85.4	35.6	37.9
325	4.50	1667	62.0	1406	25.7	84.4	97.5	60.1	88.6	96.2	85.1	37.3	40.5
325	4.75	1762	70.6	1516	29.8	85.6	97.0	59.3	90.7	96.2	85.4	38.1	40.4
325	5.00	1872	73.9	1508	29.2	82.7	97.2	59.8	91.1	95.4	86.0	37.7	39.5
325	5.25	1979	79.7	1548	30.6	80.6	96.5	55.1	91.8	93.8	86.6	34.1	34.8

4.2.2 Magnetically Shielded Thruster Performance

Testing of the magnetically shielded (MS) configuration of the CSU Hall thruster was performed in March of 2020 directly following the cathode comparison test campaign in February. The same test procedure was followed for the Magnetically Shielded configuration of the thruster, although time constraints only allowed testing with a center mounted cathode, and

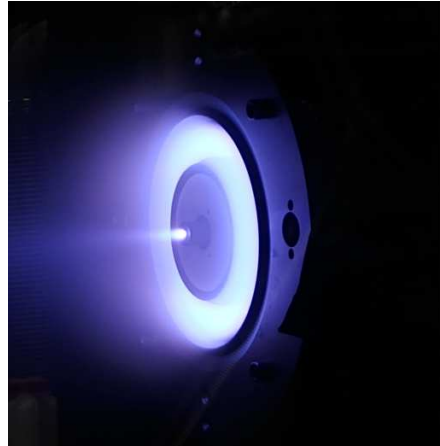


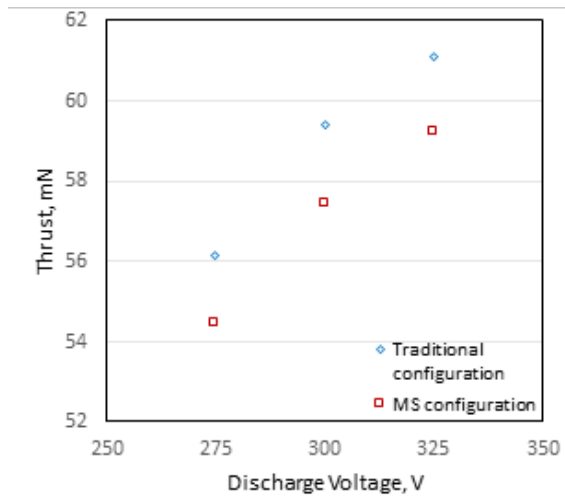
Figure 4.16: Magnetically shielded configuration of the thruster running during the test campaign

technical issues and the sudden disruption caused by the COVID-19 pandemic prevented the use of the Faraday probe for the full range of operating set-points. The thruster is shown running in the magnetically shielded configuration in Fig. 4.16. A striking difference in physical appearance of the plasma in the channel was not noted between the traditional and MS configurations, but any actual difference might have been subtle and difficult to notice with the naked eye for this relatively small thruster.

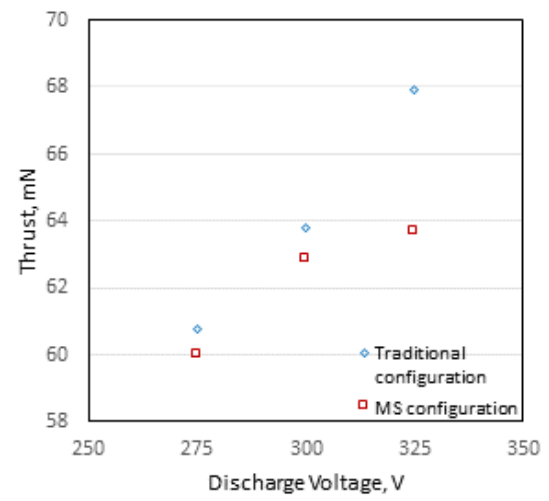
Thrust produced by the magnetically shielded thruster is compared to the thrust produced in the traditional configuration in Fig. 4.17, where both used the center mounted cathode. Thrust generally increased with increasing discharge voltage as expected. At 325V discharge, some flowrates did not follow the linear trend typically seen, and at 5.0 mg/s the thrust actually decreased compared to the same flowrate at 300V discharge. This anomalous data point is likely the result of non-optimization of the magnetic field, due to the imperfect nature of the procedure for determining the optimal coil currents, however, this could also indicate that the 325V discharge voltage may not be optimal for the thruster in the MS configuration. The thrust produced by the MS thruster ranged from 54.5 mN to 80.5 mN \pm 1.5 mN. The MS configuration produced lower thrust than the traditional configuration in all cases, with an average difference of 2.25 mN.

Anode specific impulse followed the same trend as thrust, as it is essentially thrust multiplied by a constant for a given mass-flow rate, so the plots are not presented. Anode I_{sp} ranged from 1348 seconds to 1648 seconds with the traditional configuration of the thruster, and from 1308 seconds to 1564 seconds with the magnetically shielded configuration, and was lower in every case for the MS configuration by an average of 48 seconds. The uncertainty in the anode specific impulse, based on the thrust measurement uncertainty, is estimated to be 3% of the calculated value.

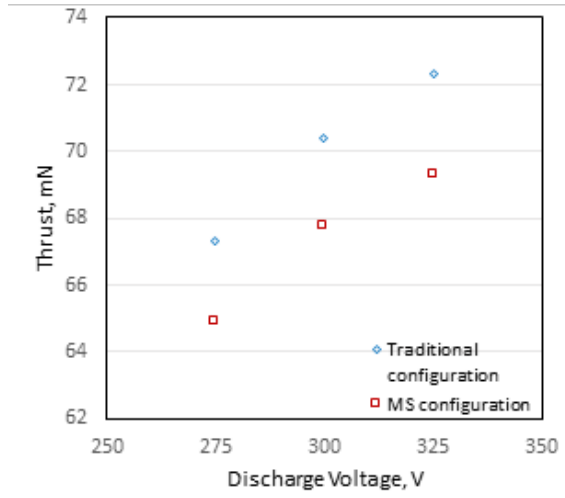
Anode efficiency for the MS and traditional configuration is plotted against discharge voltage in Fig. 4.18. Anode efficiency with the traditional configuration ranged from 28.5% to 34.8%, and with the magnetically shielded configuration it ranged from 27.6% to 33.4%. In all but one case, the MS configuration produced lower anode efficiency. Lower efficiency at 325V compared to 300V is seen in all cases with the MS thruster. This could be due to improper optimization of the magnetic field, but could also indicate that thruster efficiency suffers at the higher discharge voltage in the MS configuration.



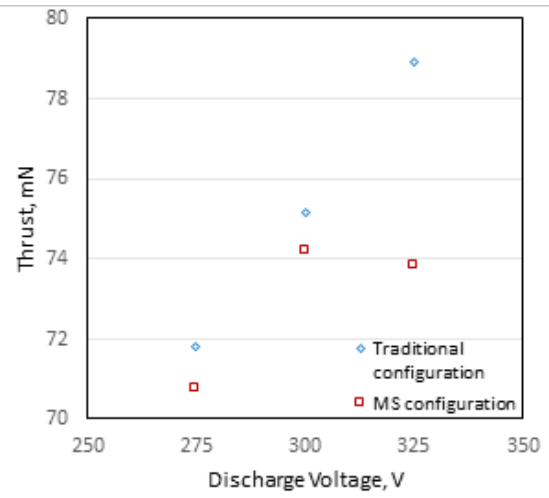
(a) 4.25 mg/s krypton



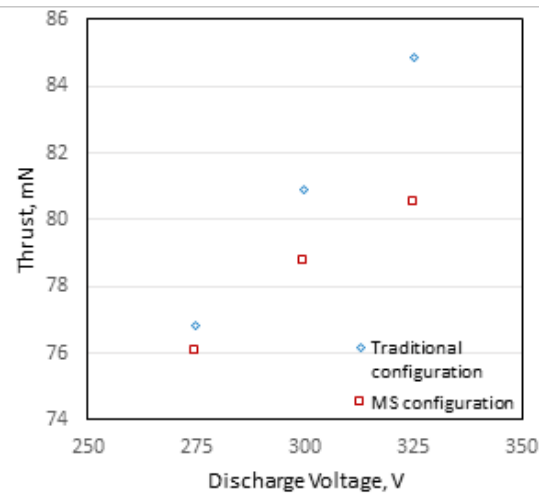
(b) 4.5 mg/s krypton



(c) 4.75 mg/s krypton

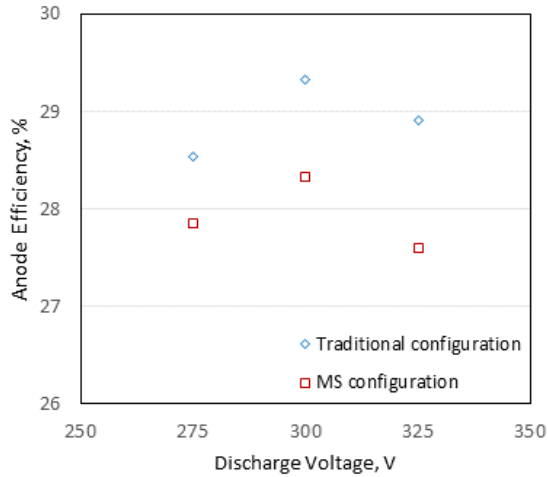


(d) 5.0 mg/s krypton

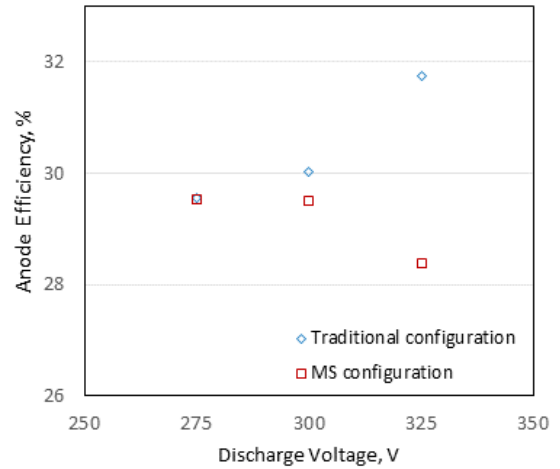


(e) 5.25 mg/s krypton

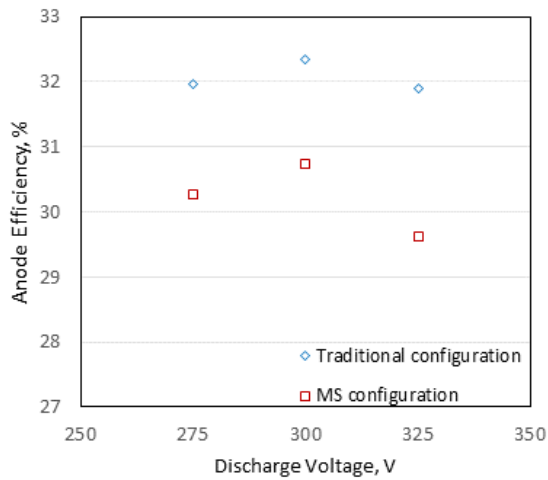
Figure 4.17: Thrust as a function of discharge voltage and anode mass flow-rate for the magnetically shielded configuration and the traditional configuration (both using center mounted cathode)



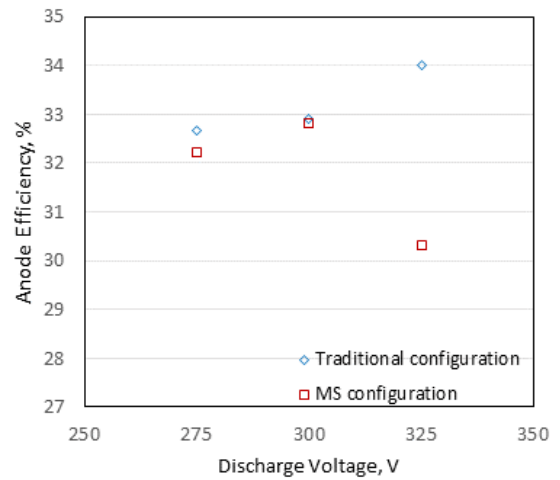
(a) 4.25 mg/s krypton



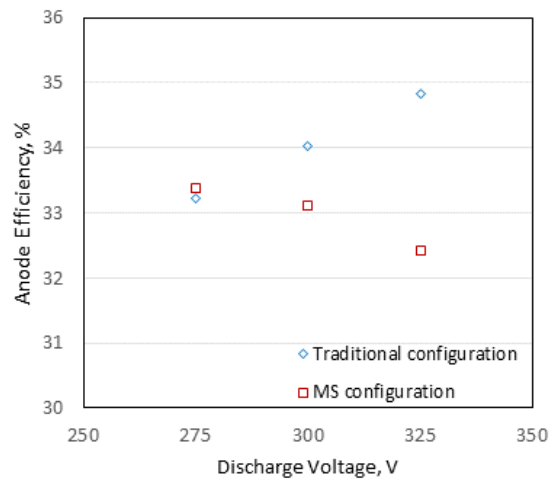
(b) 4.5 mg/s krypton



(c) 4.75 mg/s krypton



(d) 5.0 mg/s krypton



(e) 5.25 mg/s krypton

Figure 4.18: Anode efficiency as a function of discharge voltage and anode mass flow-rate for the magnetically shielded configuration and the traditional configuration (both using center mounted cathode)

A comparison of the ESA traces taken at 300V, 4.75 mg/s for both the traditional configuration and magnetically shielded configuration is shown below in Fig. 4.19. The trace for the magnetically shielded configuration exhibits a significantly larger low-energy shoulder. In this case, the most probable energy in both configurations was 290 eV, however some of the operating conditions produced most probable energies differing by a few electron-volts.

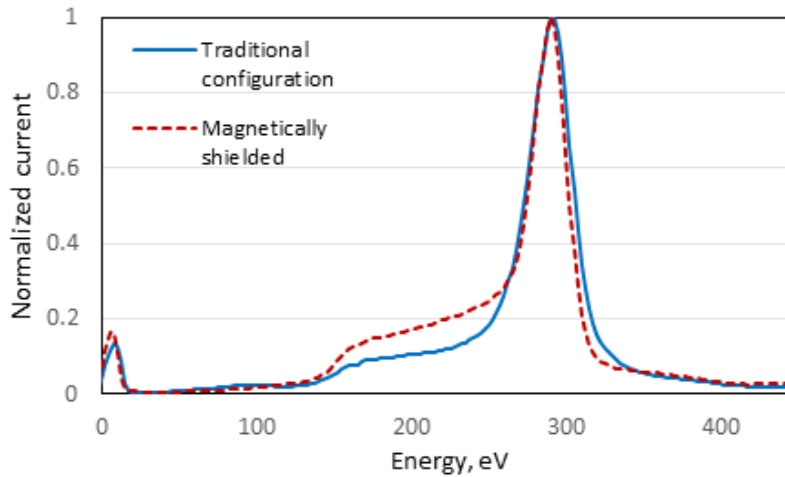
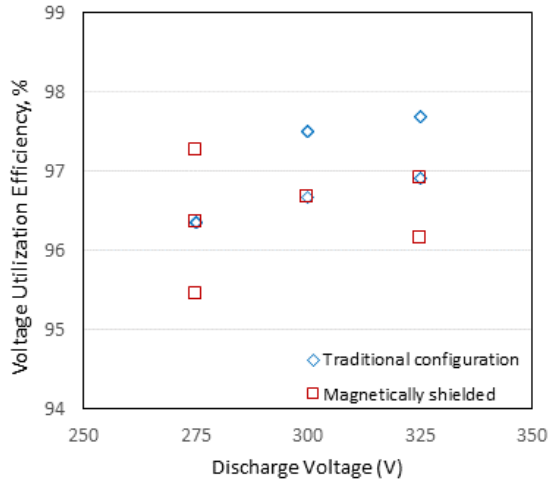
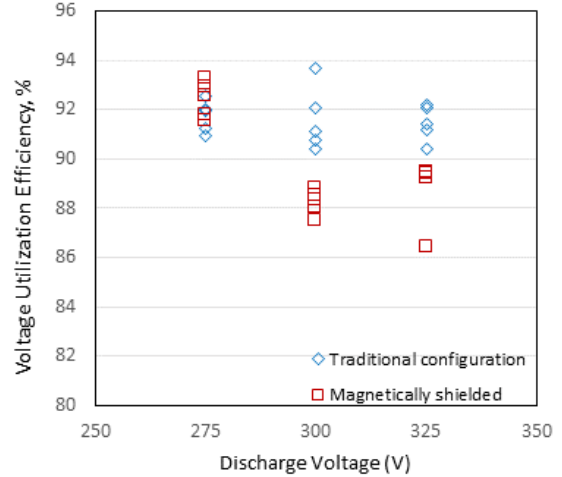


Figure 4.19: ESA traces at 300V, 4.75 mg/s with the traditional and magnetically shielded configurations, both using the center-mounted cathode

The voltage utilization efficiencies for all cases, calculated with both the most probable ion energy and the average ion energy, are shown in Fig. 4.20. When calculated with the most probable ion energy, voltage efficiency ranged from 96.4% to 97.7% in the traditional configuration, and from 95.5% to 97.3% in the magnetically shielded configuration. When using the average ion energy to calculate voltage utilization, the traditional configuration ranged from 90.4% to 93.7%, and the magnetically shielded configuration ranged from 86.4% to 93.2%. With both calculation methods, the traditional configuration outperformed in a majority of cases, however, at 275V the magnetically shielded configuration produced higher average ion energy at all flow rates, and higher most probable energy at one, 4.25 mg/s.



(a) Calculated with the most probable ion energy



(b) Calculated with the average ion energy

Figure 4.20: Voltage utilization efficiency calculated with the most probable energy and average energy vs. discharge voltage for the traditional and magnetically shielded configurations

Unfortunately, issues with the data acquisition system for the Faraday probe and then the CSU-wide shut down of labs due to the COVID-19 pandemic prevented the collection of Faraday probe data for all but six of the operating conditions with the magnetically shielded thruster configuration. This, in turn, prevented calculation of current utilization and mass utilization efficiencies for those operating conditions. However, the available data points (all flow rates at 275V, and 4.25 mg/s at 300V) will be presented. The comparison of the Faraday probe traces for both configurations is shown in Fig. 4.21. The peak current density with the MS configuration was slightly lower, and the current between -30 and -60 degrees and between +30 and +60 degrees was also slightly lower.

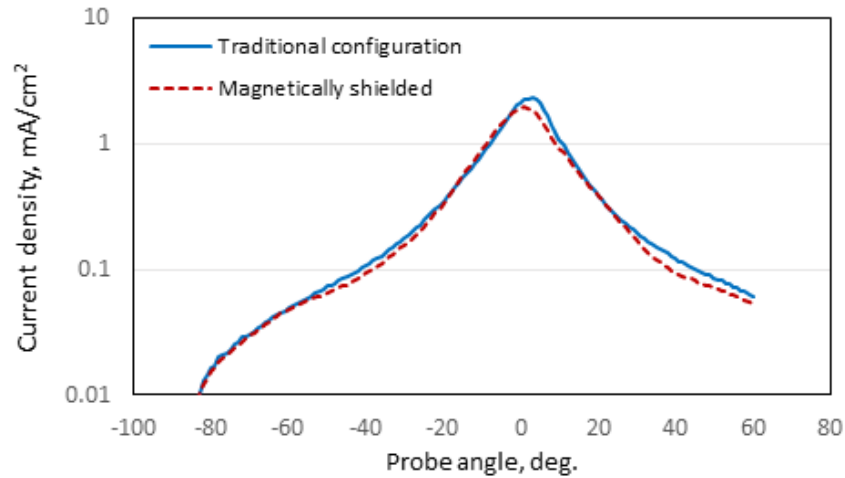
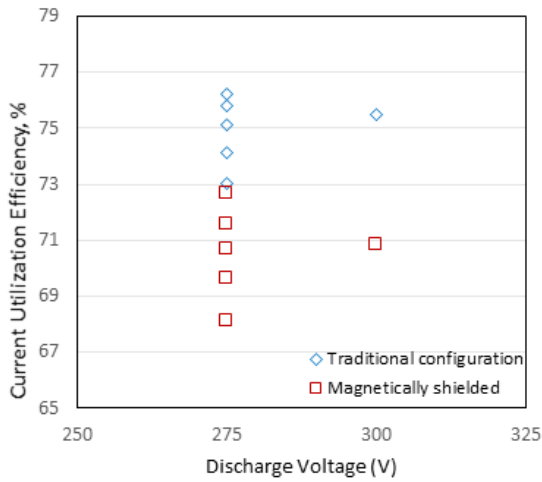


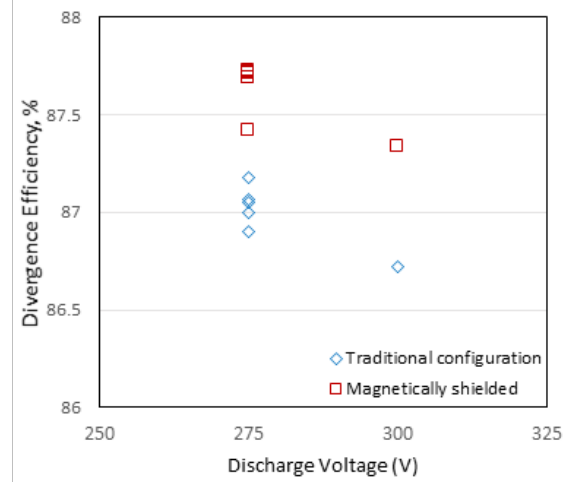
Figure 4.21: Faraday probe traces at 275V, 4.75 mg/s with the traditional and magnetically shielded configurations

The lower peak current seen in Fig. 4.21 was seen at the other operating conditions as well, resulting in lower beam current with the magnetically shielded configuration. Discharge current was also generally lower at a given operating condition with the MS configuration, but not enough to make up for the lower beam current in terms of efficiency. The current utilization efficiencies calculated from the Faraday probe data are shown in Fig. 4.22a. Current utilization ranged from 73.0% to 76.2% with the traditional configuration, and from 68.1% to 72.7% with the magnetically shielded configuration. The efficiency was lower for every case with the magnetically shielded thruster.

On the other hand, plume divergence angle was lower for all cases with the magnetically shielded configuration, resulting in higher divergence efficiency, which is shown in Fig. 4.22b. This is in contrast to the findings in [40], in which magnetic shielding produced higher plume divergence. This discrepancy may be due to the differences in the particular design of the magnetic field between these two cases.



(a) Current utilization



(b) Divergence efficiency

Figure 4.22: Current utilization and divergence efficiencies vs. discharge voltage for the HET in traditional and magnetically shielded configurations

Figure 4.23 shows the $E \times B$ probe trace for both configurations at the 300V, 4.75 mg/s operating point. The traces are a very close match, however the magnetically shielded configuration exhibited more 'blending' between the first and second peaks, a slightly lower second peak (doubly charged ions), and a slightly larger third peak (triply charged ions).

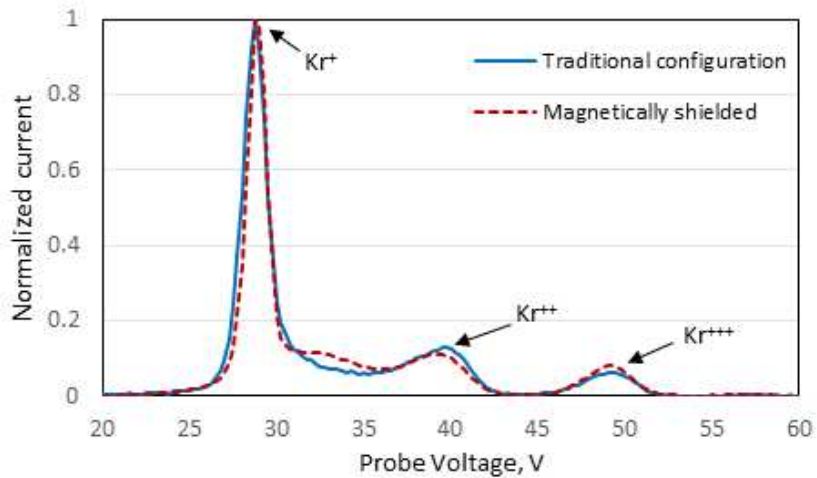


Figure 4.23: $E \times B$ traces at 300V, 4.75 mg/s with the traditional and magnetically shielded configurations

The charge utilization efficiency is shown plotted against discharge voltage in Fig. 4.24a. Charge utilization efficiency ranged from 96.2% to 97.7% for the traditional configuration and from 96.1% to 98.1% with the magnetically shielded configuration. The average charge utilization efficiencies at each discharge voltage were 96.8%, 97.2%, and 97.3% respectively for the traditional configuration, and 96.8%, 97.4%, and 97.1% for the magnetically shielded configuration. This indicates that the two configurations were very similarly efficient in ionization of the propellant, and that there is not a very strong trend between discharge voltage and charge utilization.

Mass utilization efficiencies for both configurations, plotted against discharge voltage, is shown in Fig. 4.24b. Mass utilization efficiency ranged from 48.2% to 52.8% for the traditional configuration and from 43.9% to 50.0% with the magnetically shielded configuration. The average mass utilization efficiency at 275V was 50.7% for the traditional configuration and 46.7% for the magnetically shielded configuration, which along with the lower efficiency at 300V, 4.25mg/s indicates that the mass utilization was generally lower with the thruster in magnetically shielded configuration.

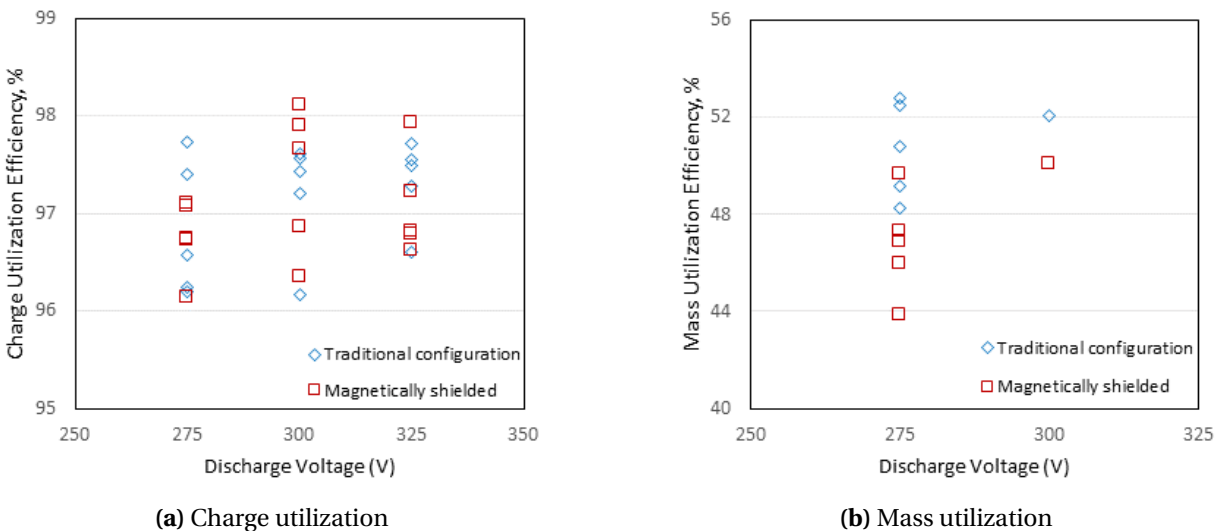


Figure 4.24: Charge and mass utilization efficiencies vs. discharge voltage for the HET in traditional and magnetically shielded configurations

Figure 4.25 shows the anode efficiency calculated using Equation 1.6 and the recorded thrust measurement, flow rate, and power (thrust-derived), in comparison with the anode efficiency calculated using Equation 1.12 and the utilization efficiencies calculated from the diagnostic probe data (probe-derived). Figure 4.25a shows the anode efficiency calculated when using the most probable ion energy in calculating the voltage utilization efficiency, while Fig. 4.25b shows the anode efficiency calculated when the average ion energy was used to calculate the voltage utilization efficiency. Contrary to the outcome with both cathodes in the traditional configuration, calculation of the voltage utilization efficiency with the most probable ion energy resulted in probe-derived anode efficiency that was a closer match to the thrust-derived efficiency. A full uncertainty analysis was not conducted for the probe data and corresponding utilization efficiencies, but as mentioned before, based on the analysis in [8], the uncertainty in the probe-derived anode efficiency is roughly 10% of the calculated value. Keeping the uncertainties in mind, the thrust-derived and probe-derived anode efficiencies for the magnetically shielded thruster are again a fairly close match.

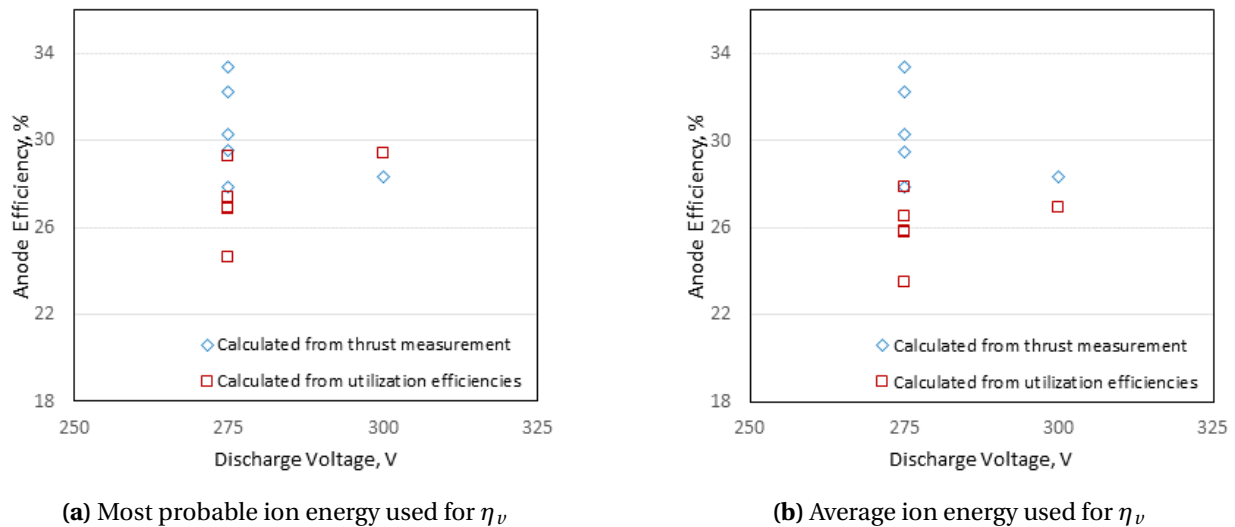


Figure 4.25: Anode efficiency vs. discharge voltage calculated using the thrust measurement, and the utilization efficiencies with the magnetically shielded configuration

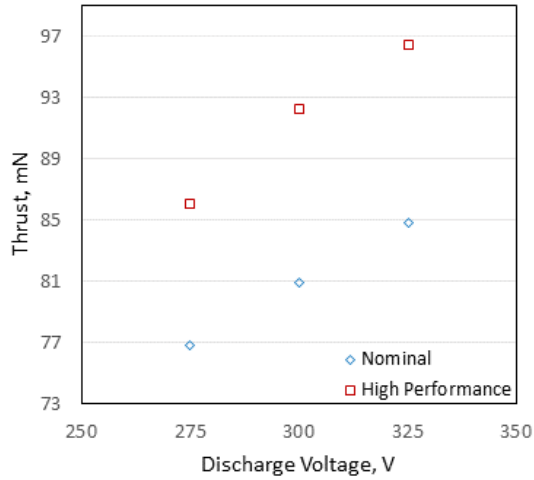
The full set of data collected with the magnetically shielded thruster configuration is shown in Table 4.5 below. because of the aforementioned issues with the collection of Faraday probe data, the parameters that were not able to be calculated are populated as 'N/A'.

Table 4.5: March 2020 test using the magnetically shielded configuration

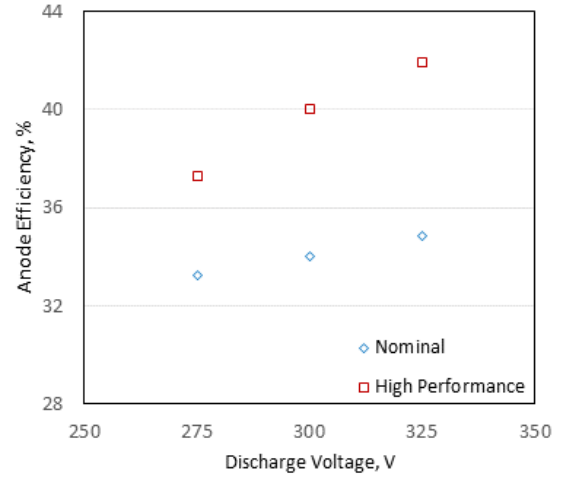
V_{anode}	\dot{m}_{anode}	P_{anode}	T	$I_{sp,anode}$	η_{anode}	η_b	η_a	η_m	$\eta_{v,avg}$	$\eta_{v,mp}$	η_d	$\eta_{a,avg}$	η_{amp}
(V)	(mg/s)	(W)	(m.N)	(s)	(%)	(%)	(%)	(%)	(%)	(%)	(%)	(%)	(%)
275	4.25	1254	54.5	1308	27.8	68.1	96.7	44.0	92.9	97.3	87.4	23.5	24.6
275	4.50	1356	60.0	1361	29.5	69.6	97.1	46.9	92.6	96.4	87.7	25.8	26.8
275	4.75	1468	64.9	1392	30.3	70.7	96.7	47.5	93.2	96.4	87.7	26.5	27.4
275	5.00	1557	70.8	1445	32.2	71.6	97.1	49.8	91.8	96.4	87.7	27.9	29.2
275	5.25	1650	76.1	1477	33.4	72.7	96.1	46.0	91.5	95.5	87.7	25.8	26.9
300	4.25	1371	57.4	1379	28.3	70.8	98.1	50.1	88.5	96.7	87.3	26.9	29.4
300	4.50	1488	62.8	1425	29.5	N/A	96.9	N/A	87.5	96.7	N/A	N/A	N/A
300	4.75	1572	67.8	1454	30.7	N/A	97.9	N/A	88.0	96.7	N/A	N/A	N/A
300	5.00	1680	74.2	1515	32.8	N/A	96.4	N/A	88.3	96.7	N/A	N/A	N/A
300	5.25	1785	78.8	1530	33.1	N/A	97.7	N/A	88.8	96.7	N/A	N/A	N/A
325	4.25	1495	59.2	1421	27.6	N/A	97.9	N/A	86.4	96.9	N/A	N/A	N/A
325	4.50	1589	63.7	1445	28.4	N/A	96.8	N/A	89.5	96.2	N/A	N/A	N/A
325	4.75	1706	69.3	1487	29.6	N/A	96.6	N/A	89.2	96.2	N/A	N/A	N/A
325	5.00	1801	73.8	1508	30.3	N/A	97.2	N/A	89.4	96.2	N/A	N/A	N/A
325	5.25	1905	80.5	1564	32.4	N/A	96.8	N/A	89.5	96.2	N/A	N/A	N/A

4.3 High Performance Mode of Operation

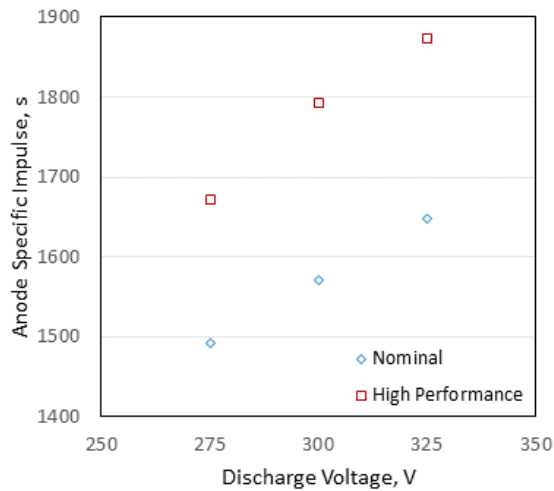
As described previously, a mode of operation providing higher thrust, specific impulse, and efficiency was discovered by increasing the magnetic field strength past the point of discharge current optimization. Data were collected at three such operating conditions during the February 2020 testing with the center-mounted cathode, shown in Fig. 4.26 compared with the data from the nominal operation.



(a) Thrust vs. discharge voltage



(b) Anode efficiency vs. discharge voltage



(c) Anode specific impulse vs. discharge voltage

Figure 4.26: Thrust, anode efficiency, and anode specific impulse in the high performance mode compared to nominal operation at 5.25 mg/s anode mass-flow rate

For each of these set-points, the inner magnetic coil power supply was set to 7A, and the outer coil was supplied with 6A. In comparison, for nominal operation the coil supplies were set to around 5.25A and 4.5A for the minimized discharge current that is standard practice. The difference in performance is obvious, with a max thrust of 96.5 mN, max anode efficiency of 42.0%, and max anode specific impulse of 1874 seconds. The error in the thrust measurement

was calculated at ± 2 mN. However the cause of this performance increase is not obvious, and analysis of data from the diagnostic probes leads to more questions.

Figure 4.27 shows the ESA trace for the 300V, 5.25 mg/s high performance mode operating condition. Instead of a narrow peak near the discharge voltage with relatively low current shoulders of high and low energy ions as seen during nominal operation, there is a much larger current of ions with energies lower and higher than the discharge voltage, resulting in a broad triangular distribution, that could be indicative of very noisy operation. The FWHM in the high performance mode is 75.2 eV, while in nominal mode FWHM is 29.6 eV. Essentially, in the high performance mode, ions are being created at a much larger range of potentials. The resulting voltage utilization efficiencies, both based on most probable ion energy and average ion energy, were slightly lower for the high performance mode.

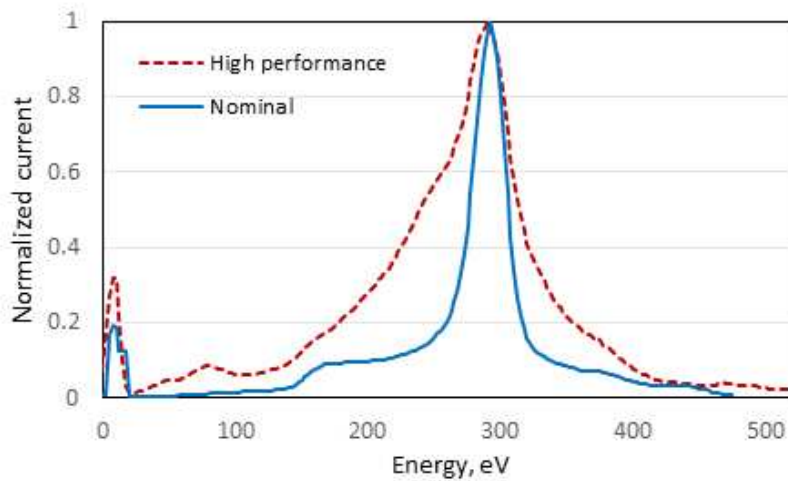


Figure 4.27: ESA probe trace at 300V, 5.25 mg/s in the high performance mode and nominal operation

The broad range of ion energies shown in the ESA trace is reflected in excessive peak 'blending' in the $E \times B$ probe trace shown in Fig. 4.28. Additionally, the $E \times B$ probe trace shows that a much larger relative concentration of doubly charged ions are being created in the high performance operation mode. This is interesting, since it leads to lower charge and mass utilization

efficiencies, and thus to lower probe derived anode efficiency, while the thrust derived efficiency was much higher than nominal operation.

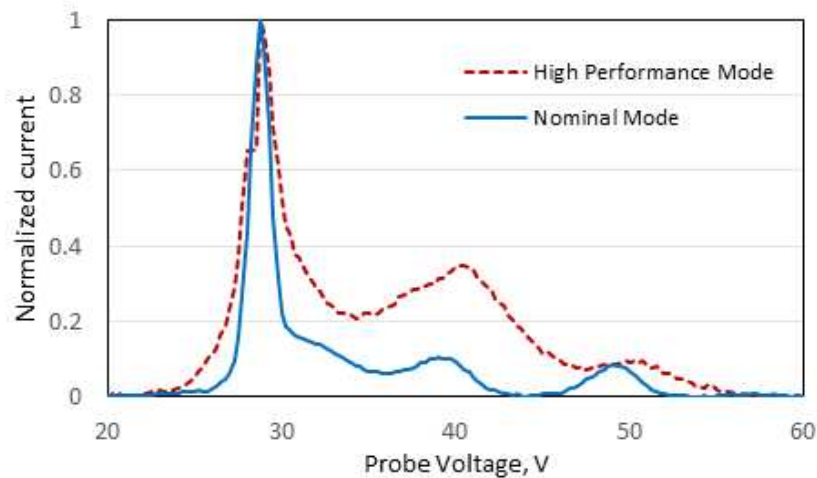


Figure 4.28: Comparison of the $E \times B$ probe trace at 300V, 5.25 mg/s during nominal operation and in the high performance mode

In an attempt to produce a more accurate calculation of the ionization species current fractions, the EVADER probe was used to collect charge state data for the 300V, 5.25 mg/s discharge operating point at set energy bands of 200, 250, 275, 300, 325, 350, 375, and 425 eV. The species current fractions were then calculated using the sum of each species current at each energy band (meant to represent the entire energy distribution), and the sum of the total current collected at each energy band. The resulting current fractions using this method were 0.53 for singles, 0.44 for doubles, and 0.037 for triples, compared to the 0.50, 0.42, 0.08 calculated with the traditional $E \times B$ probe. This brings the charge and mass utilization up slightly, but not by a significant amount, and it is not known which result is more accurate. Examples of the EVADER traces at selected energies of 250 eV and 300 eV are shown in Fig. 4.29. Even though the traces themselves are spectacular examples in terms of eliminating the peak broadening seen with traditional $E \times B$ probes, the preliminary analysis done here did not result in significantly different charge and mass utilization efficiency values.

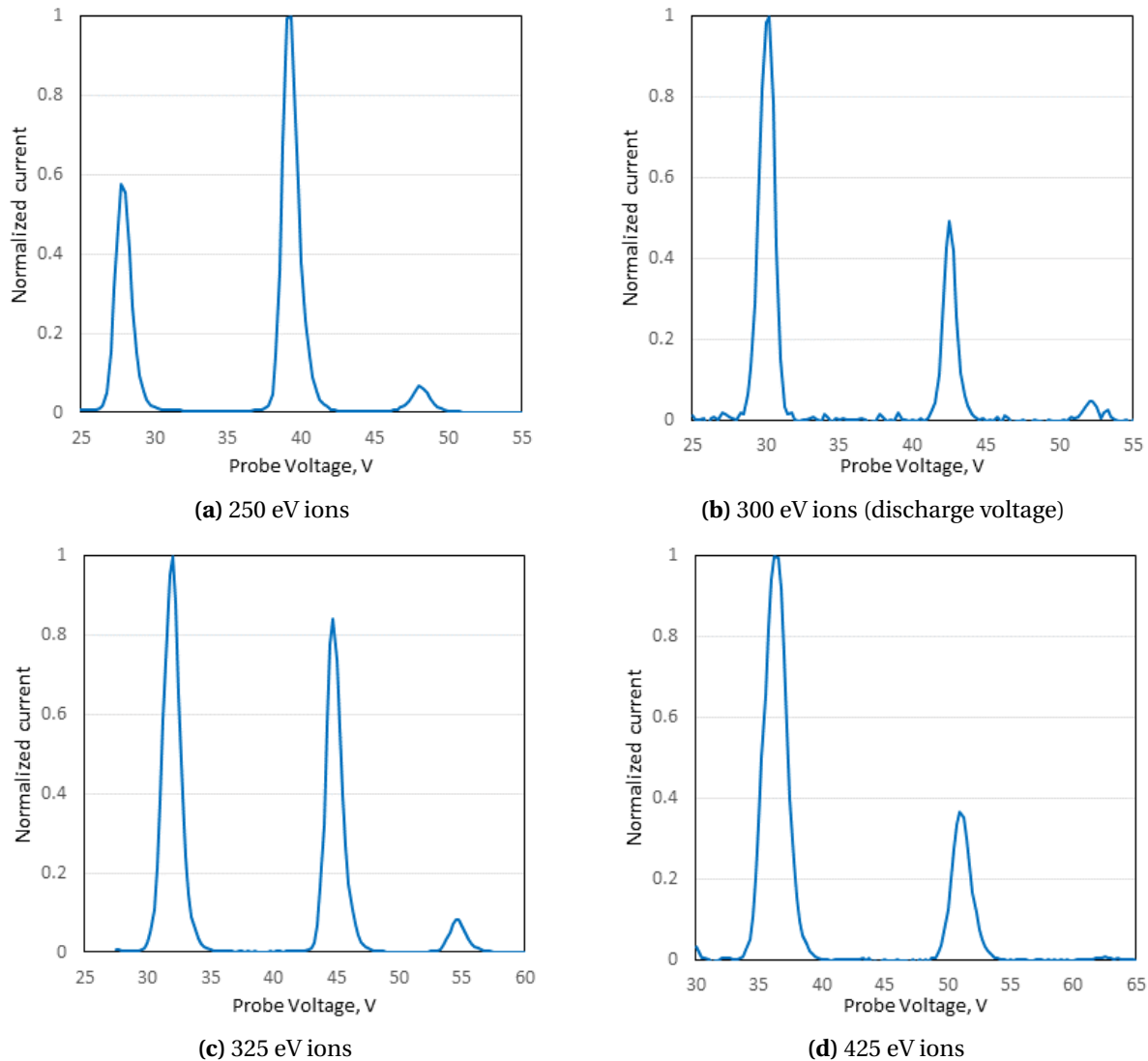


Figure 4.29: EVADER probe traces at selected ion energies in the high performance mode at 300V, 5.25 mg/s

The ions with energies in the triangular part of the IEDF shown previously in Fig. 4.27, represented by the 250 and 325 eV energy band traces shown above, seem to have much higher concentrations of doubly charged ions than typical. However, the very high energy ions at 425 eV are mostly singly charged. This information does not give insight into any particular reasons for the high performance operation, but is interesting nonetheless. Collection of EVADER data at a larger number of energy bands could likely provide deeper insight, but time constraints prevented further investigation.

Data collected by the Faraday probe show a higher beam current, corresponding with the higher discharge current in this mode as compared to the minimized discharge current in standard operation. The high performance mode shows slightly higher current utilization efficiency, but lower divergence efficiencies, shown in Fig. 4.30. This means that the high performance mode is only creating a slightly higher beam current for a given discharge current, and that the ions in the beam have, in general, more radial velocity than the beam ions during nominal operation.

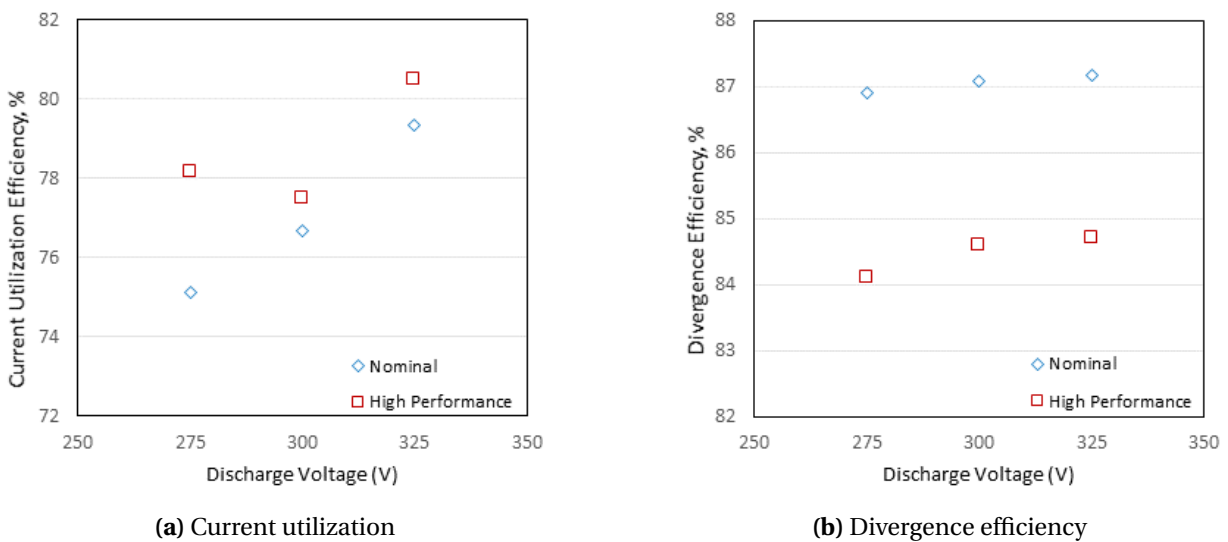


Figure 4.30: Current utilization and divergence efficiencies vs. discharge voltage for the HET in high performance mode and nominal operation

The probe-derived anode efficiency is compared to the thrust-derived anode efficiency in Fig. 4.31. As the data show, the probe-derived efficiency is significantly lower than the thrust derived efficiency, and does not reflect "high performance". In fact, the probe-derived efficiencies are very much in-line with the efficiencies seen during nominal operation. This raises many questions, first and foremost whether the thrust measurements for the high performance (presumably noisy) mode can be believed. More investigation is required to come to a clear conclusion regarding this high performance mode, but as there is a visible difference noted in the plasma plume, and that similar thrust measurements have been repeated at least twenty

times now, we do believe that the thrust measurements are valid. New methods of analyzing the diagnostic probe data may need to be developed to produce more accurate results describing the physical mechanisms at work.

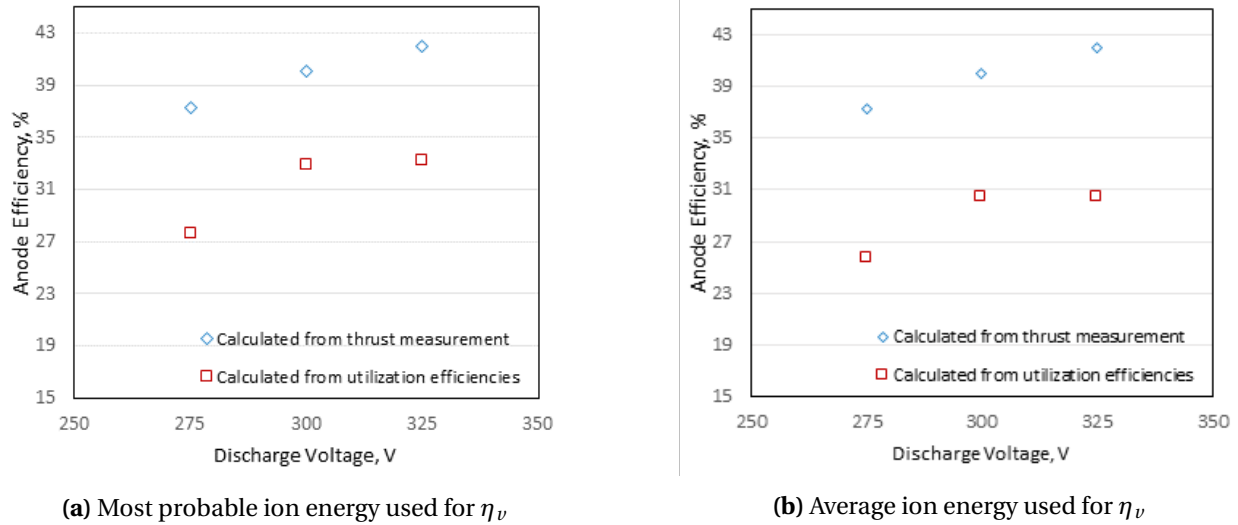


Figure 4.31: Anode efficiency vs. discharge voltage calculated using the thrust measurement, and the utilization efficiencies for the high performance data-points

The set of data collected in the high performance mode of operation is shown in Table 4.6 below.

Table 4.6: High performance operation mode data set

V_{anode}	\dot{m}_{anode}	P_{anode}	T	$I_{sp,anode}$	η_{anode}	η_b	η_a	η_m	$\eta_{v,avg}$	$\eta_{v,mp}$	η_d	$\eta_{s,avg}$	$\eta_{s,mp}$
(V)	(mg/s)	(W)	(mN)	(s)	(%)	(%)	(%)	(%)	(%)	(%)	(%)	(%)	(%)
275	5.25	1892	86.0	1671	37.3	78.2	96.3	45.3	89.4	96.4	84.1	25.6	27.6
300	5.25	2025	92.3	1792	40.0	77.5	96.5	53.8	89.3	96.7	84.6	30.4	32.9
325	5.25	2113	96.5	1873	41.9	80.5	96.2	52.3	88.8	96.9	84.7	30.5	33.2

Chapter 5

Conclusion and Future Work

5.1 Conclusion

A study was conducted on the performance differences of laboratory krypton Hall thruster operating with a center-mounted cathode and an outer-pole-piece mounted cathode (the postage stamp) was conducted. The first set of data, collected in April 2019, showed that thrust, efficiency, and specific impulse were all generally lower when using the postage stamp cathode, however, this was not the case for all operating conditions, and the difference was typically within the experimental uncertainty. The second set of data, collected in February 2020, showed a more conclusive trend of lower thrust, efficiency, and specific impulse at all operating conditions for the pole-piece mounted cathode, and the difference in performance was generally outside of the estimated error. Electrostatic analyzer data showed a clear trend of lower voltage utilization efficiency when using the postage stamp cathode. Faraday probe data showed higher current utilization efficiency with the postage stamp, and, conversely, higher divergence efficiency with the center-mounted cathode. Data from the E×B probe resulted in very similar charge utilization efficiencies, but a slight trend of higher mass utilization efficiency with the postage stamp cathode. When comparing the thrust-derived and probe-derived anode efficiencies, the results matched closely in all cases except at 325V with the postage stamp. At this discharge voltage, high beam current was measured with the postage stamp that resulted in significantly higher probe-derived anode efficiency. Since all other operating conditions matched much more closely, we are skeptical of this result, and further investigation of operation at 325V should be conducted with the Faraday probe. In general, these results suggest that performance of the Hall thruster does generally suffer when using the postage stamp cathode, mounted to the outer pole-piece of the thruster, as compared to operation with the center-mounted cathode. However, when considering the potential benefits of the postage stamp cathode geometry

and mounting location, it may still be worth the small loss in overall thruster performance in certain applications. For example, a postage-stamp-style cathode could ease the scaling of Hall Effect thrusters to higher power levels by allowing multiple cathodes to be placed on the pole pieces of nested Hall thrusters rather than utilizing one large, high-current, center-mounted cathode. Likewise, a postage stamp style cathode might also be easier to integrate onto a miniaturized Hall thruster meant for cubesat class spacecraft, where available space in the center of the thruster might be severely limited.

Additionally, the performance of the Hall thruster in the magnetically shielded configuration was tested and compared with the traditional configuration, both using the center mounted cathode. Thrust was lower in the MS configuration in all cases, though frequently within the estimated error. Anode efficiency was lower in all cases but one, but also within the error in many cases. Specific impulse was lower in all cases. It seems that performance is generally slightly lower with the MS configuration. Data from the electrostatic analyzer showed that the MS configuration was generally less efficient in accelerating the beam ion, although at 275V it produced higher average ion energies. Additionally, Faraday probe data showed that the MS thruster had lower current utilization efficiency, but higher divergence efficiency, than the traditional configuration. $E \times B$ probe data resulted in very similar charge utilization between the two configurations, but generally lower mass utilization for the MS configuration. The probe data and utilization efficiencies corroborate the indication that the magnetically shielded thruster suffers a small performance loss compared to the traditional configuration. When comparing the anode efficiency calculated using the thrust measurement and using the utilization efficiencies, the results are within the estimated uncertainty, but are closest when the most probable ion energy is used to calculate voltage utilization efficiency, rather than the average ion energy. This is because the most probable ion energy was always higher than the average, giving a higher voltage utilization efficiency, and 'making up' for the low current and mass utilization efficiencies.

Last, an initial investigation of the high performance operation mode of the traditional configuration Hall thruster was conducted. During the February 2020 test using the center-

mounted cathode, this mode produced maximums of 96.5 mN thrust, 42.0% anode efficiency, and 1874 seconds of anode specific impulse, however, data collected with the diagnostic probes did not show any obvious causes of this higher performance, and the probe-derived anode efficiency was much lower than the thrust-derived, and was in line with the anode efficiency seen under nominal operation. A new probe termed the EVADER, created by Plasma Controls, LLC., was also used to study the high performance mode. This probe allows one to eliminate the blending between peaks typically seen in traditional $E \times B$ probe traces by filtering ions first by their energy, and then by their velocity. Analysis of the data collected with the EVADER probe showed slightly higher charge and mass utilization efficiencies, but the overall probe-derived anode efficiency was still significantly lower than the thrust-derived efficiency. Further detailed investigation will be required to determine the physical explanation for this anomalous operation mode.

5.2 Future Work

5.2.1 Further Investigation of the High Performance Mode

A much more thorough study must be conducted to uncover what causes the marked higher performance of the thruster under high magnetic field, and whether these data can be believed. To make the thrust measurement and thrust-derived efficiencies credible, we believe that matching results from the diagnostic probe derived efficiency would be necessary.

5.2.2 Magnetic Field Mapping

Conducting a detailed mapping of the magnetic field created by the electromagnetic coils would be an important first step in continuing Hall thruster research at CSU. Through the use of a motion stage and a Gauss probe, one could measure the magnetic field at a large number of points and create a detailed map of the field, which could then be repeated at monthly intervals to ensure the magnetic circuit is still working properly.

5.2.3 Magnetically Shielded Thruster Plume Characterization

Unfortunately, issues with the Faraday probe data acquisition system and then the subsequent shut-down of the lab due to the COVID-19 pandemic prevented full characterization of the plume produced by the magnetically shielded configuration of the thruster. To further understand the operation of the thruster in this configuration, Faraday probe data needs to be collected for the entire range of voltages and flow rates.

5.2.4 Hall Current Tomography

The Hall current tomography sensor is a CEPPE lab developed tool used to quantitatively image the Hall current, the circulating current of electrons in the thruster channel. The sensor uses 8 tunneling-magneto-resistive sensors to measure the magnetic field induced by the Hall current. This measurement of the induced field can then be used to solve the inverse magnetostatic problem and calculate the current density of the Hall current. This current density calculation can be spatially and temporally resolved to provide two dimensional tomography images and videos of the Hall current as it changes over time. A thorough description of the development and initial testing of the tool is given by Mullins [41]. Data were collected using the sensor during this thesis research project, but time constraints and issues with the MATLAB scripts used to process the data prevented analysis from being completed. Analysis of these data could provide further insight into the physical mechanisms affecting Hall thruster performance, and, for the MS configuration, would be the first time, to our knowledge, that the Hall current in a magnetically shielded thruster has been imaged in a non-intrusive manner.

5.2.5 Thruster upgrades

Several upgrades to the thruster could improve the ease of disassembly and re-assembly, and quicken the pace of testing. One such upgrade would be to wire all electrical connections to a single 6-pin connector, which would speed up mounting of the thruster and also help prevent mixing up electrical connections. Additionally, the center coil of the thruster is currently slightly

too large, resulting in considerable difficulty in centering the coil properly. A thinner sleeving for the copper wire would solve this issue, but the sleeving must still be able to protect the coil from the high temperatures encountered in this region. Fabrication of a new thruster channel may also improve performance of the thruster, as the downstream end of the existing channel has been eroded through years of operation.

Bibliography

- [1] D. Goebel and I. Katz. *Fundamentals of Electric Propulsion*, volume 3. John Wiley & Sons, Inc., NJ, USA, 2008.
- [2] Edgar Choueiri. A Critical History of Electric Propulsion: The First Fifty Years (1906-1956). *Journal of Propulsion and Power*, pages 193–203, 2004.
- [3] R.H. Goddard. Method and means for producing electrically-charged particles. US Patent No. 1,137,964, May 1915.
- [4] Hermann Oberth. *Wege zur Raumschiffahrt. (German) [Ways to Spaceflight]*. Druck und Verlag von R. Oldenbourg, Munich and Berlin, Germany, 1929.
- [5] V.V. Zhurin, A.A. Porotnikov, and V.P. Shadov. Electric propulsion research and development in the USSR. In *AIAA International Electric Propulsion Conference*, Key Biscayne, FL, 1976. AIAA 1976-1073.
- [6] Dan Lev, Roger M. Myers, Kristina M. Lemmer, Jonathan Kolbeck, Michael Keidar, Hiroyuki Koizumi, Han Liang, Daren Yu, Tony Schonherr, Jose Gonzalez del Amo, Wonho Choe, Riccardo Albertoni, Andrew Hoskins, Shen Yan, William Hart, Richard R. Hofer, Ikkoh Funaki, Alexander Lovtsov, Kurt Polzin, Anton Olshanskii, and Olivier Duchemin. The technological and commercial expansion of electric propulsion in the past 24 years. In *35th International Electric Propulsion Conference*, Atlanta, GA, 2017.
- [7] Richard Hofer. *Development and Characterization of High-Efficiency, High-Specific Impulse Xenon Hall Thrusters*. PhD thesis, Department of Aerospace Engineering, University of Michigan, Ann Arbor, MI, 2004.
- [8] Wensheng Huang, Rohit Shastry, George C. Soulas, and Hani Kamhawi. Farfield plume measurement and analysis on the nasa-300m and nasa-300ms. In *33rd International Electric Propulsion Conference*, Washington, D.C., 2013.

- [9] Yassir Azziz. *Experimental and Theoretical Characterization of a Hall Thruster Plume*. PhD thesis, Department of Aeronautics and Astronautics, Massachusetts Institute of Technology, Cambridge, MA, 2007.
- [10] Richard Hofer and Alec Gallimore. Efficiency analysis of a high-specific impulse Hall thruster. In *40th AIAA/ASME/SAE/ASEE Joint Propulsion Conference*, Fort Lauderdale, FL, 2004. AIAA 2004-3602.
- [11] Dan Lev and Leonid Appel. Heaterless hollow cathode technology - a critical review. In *Space Propulsion 2016*, Rome, Italy, 2016. SP2016_3125366.
- [12] M.F. Schatz. Heaterless ignition of inert gas ion thruster hollow cathodes. In *AIAA/DGLR/JSASS 18th International Electric Propulsion Conference*, Alexandria, VA, 1985. AIAA-85-2008.
- [13] Ryan K. Ham, John D. Williams, Scott J. Hall, Gabriel F. Benavides, and Timothy R. Verhey. Characterization of a fixed-volume release system for initiating an arc discharge in a heaterless hollow cathode. In *36th International Electric Propulsion Conference*, Vienna, Austria, 2019.
- [14] Graeme Aston. Hollow cathode startup using a microplasma discharge. *Review of Scientific Instruments*, 52:1259 – 1260, 1981.
- [15] V. Vekselman, Ya. E. Krasik, S. Gleizer, V. Tz. Gurovich, A. Warshavsky, and L. Rabinovich. Characterization of a heaterless hollow cathode. *Journal of Propulsion and Power*, 29(2), 2013.
- [16] B.A. Arkhipov. Development and research of heaterless cathode-neutralizer for linear Hall thrusters (LHD) and plasma ion thrusters (PIT). In *25th international Electric Propulsion Conference*, Cleveland, OH, 1997. IEPC-97-175.

- [17] Dan Lev, Gal Alon, Leonid Appel, Omri Seeman, and Yoav Hadas. Low current heaterless hollow cathode development overview. In *35th International Electric Propulsion Conference*, Atlanta, GA, 2017. IEPC-2017-244.
- [18] R. Albertoni, M. Andrenucci, D. Pedrini, and F. Paganucci. Preliminary characterization of a lab₆ hollow cathode for low-power Hall effect thrusters. In *33rd International Electric Propulsion Conference*, Washington, D.C., 2013. IEPC-2013-137.
- [19] L. Albarede, V. Lago, P. Lasgorceix, M. Dudeck, A. Burgova, and K. Malik. Interaction of a hollow cathode stream with a Hall thruster. In *28th International Electric Propulsion Conference*, IEPC-2003-333, Toulouse, France, 2003.
- [20] N. Koshalev and A. Loyan. Investigation of hollow cathode for low power Hall effect thruster. In *30th International Electric Propulsion Conference*, IEPC-2007-103, Florence, Italy, 2007.
- [21] A. Loyan, M. Titov, O. Rybalov, and T. Maksymenko. Middle power Hall effect thrusters with centrally located cathode. In *33rd International Electric Propulsion Conference*, IEPC-2013-410, Washington, D.C., 2013.
- [22] V. Murashko, A. Koryakin, A. Nesterenko, S. Olotin, A. Oranskiy, A. Loyan, M. Koshelev, V. Bilokon, and S. Nesterenko. Russian flight Hall thrusters spt-70 & spt-100 after cathode change start during 20-25ms. In *30th International Electric Propulsion Conference*, IEPC-2007-62, Florence, Italy, 2007.
- [23] R. Hofer, L. Johnson, D. Goebel, and R. Wirz. Effects of internally mounted cathodes on Hall thruster plume properties. *IEEE Transactions on Plasma Science*, 36(5), 2008.
- [24] J. Sommerville and L. King. Hall-effect thruster – cathode coupling part i: Efficiency improvements from an extended outer pole. *Journal of Propulsion and Power*, 27(4), 2011.
- [25] K. Jameson, D. Goebel, R. Hofer, and R. Watkins. Cathode coupling in Hall thrusters. In *30th International Electric Propulsion Conference*, IEPC-2011-003, Florence, Italy, 2007.

- [26] Casey Farnell, Cody Farnell, J. Williams, D. Williams, B. Nguyen, K. Greiner, and R. Ham. Simplified formation process of a low work function insert. U.S. Patent 10002738, 2018.
- [27] Daniel L. Brown, Mitchell L. R. Walker, James Szabo, Wensheng Huang, and John E. Foster. Recommended practice for use of faraday probes in electric propulsion testing. *Journal of Propulsion and Power*, 33(3), 2017.
- [28] J.L. Rovey, M.L.R. Walker, P.Y. Peterson, and A.D. Gallimore. Magnetically filtered faraday probe for measuring the ion current density profile of a Hall thruster. *Review of Scientific Instruments*, 77(1), 2006.
- [29] Casey C. Farnell, Cody C. Farnell, Shawn C. Farnell, and John D. Williams. Recommended practice for use of electrostatic analyzers in electric propulsion testing. *Journal of Propulsion and Power*, 33(3):638–658, 2017.
- [30] Casey C. Farnell, Cody C. Farnell, Shawn C. Farnell, and John D. Williams. Electrostatic analyzers with application to electric propulsion testing. In *33rd International Electric Propulsion Conference*, Washington, D.C., 2013. IEPC 2013-300.
- [31] Casey C. Farnell, Daniel L. Brown, Garret Willis, Richard Branam, and John D. Williams. Remote diagnostic measurements of Hall thruster plumes. In *31st International Electric Propulsion Conference*, Ann Arbor, MI, 2009. IEPC 2009-031.
- [32] Rohit Shastry, Richard R. Hofer, Bryan M. Reid, and Alec D. Gallimore. Method for analyzing $e \times b$ probe spectra from hall thruster plumes. *Review of Scientific Instruments*, 80, 2009.
- [33] Brian Beal. *Clustering of Hall Effect Thrusters for High-Power Electric Propulsion Applications*. PhD thesis, Department of Aerospace Engineering, University of Michigan, Ann Arbor, MI, 2004.
- [34] I.G. Mikellides, I. Katz, Richard R. Hofer, and Dan M. Goebel. Magnetic shielding of walls from the unmagnetized ion beam in a Hall thruster. *Applied Physics Letters*, 102, 2013.

- [35] I.G. Mikellides, I. Katz, Richard R. Hofer, and Dan M. Goebel. Magnetic shielding of a laboratory Hall thruster. I. Theory and validation. *Journal of Applied Physics*, 115, 2014.
- [36] Richard R. Hofer, Dan M. Goebel, I.G. Mikellides, and I. Katz. Magnetic shielding of a laboratory Hall thruster. II. Experiments. *Journal of Applied Physics*, 115, 2014.
- [37] Rafael Martinez, John Williams, J.J. Moritz, and Casey Farnell. Hall current plasma source having a center-mounted cathode or a surface-mounted cathode. U.S. Patent 10269526, 2019.
- [38] James E. Polk, Anthony Pancottie, Thomas Haag, Scott King, Mitchell Walker, Joseph Blakely, and John Ziemer. Recommended practice for thrust measurement in electric propulsion testing. *Journal of Propulsion and Power*, 33(3), 2017.
- [39] M. Nakles, W. Hargus, J. Delgado, and R. Corey. A performance comparison of xenon and krypton propellant on an spt-100 hall thruster. In *32nd International Electric Propulsion Conference*, Weisbaden, Germany, 2011.
- [40] Richard R. Hofer, Dan M. Goebel, Ioannis G. Mikellides, and Ira Katz. Design of a laboratory hall thruster with magnetically shielded channel walls, phase ii: Experiments. In *48th AIAA/ASME/SAE/ASEE Joint Propulsion Conference & Exhibit*, Atlanta, GA, 2012.
- [41] Carl Mullins. A non-invasive Hall current distribution measurement system for hall effect thrusters. Master's thesis, Department of Mechanical Engineering, Colorado State University, Fort Collins, CO, 2015.